

Spatiotemporal Hysteresis Distribution and Decomposition of Solar Activities and Climatic Oscillation during 1900-2020

Mingyang Li¹, Tingxi Liu¹, Long Ma¹, Limin Duan¹, Yixuan Wang¹, Guoqiang Wang², Huimin Lei³, and Vijay P Singh⁴

¹Inner Mongolia Agricultural University

²Beijing Normal University

³Tsinghua University

⁴Texas A&M University

November 22, 2022

Abstract

Meteorological elements have different lag periods for solar activities (SA), climatic oscillation (CO) and other influencing factors at different spatiotemporal scales. To further understand the “solar-climate-water resource” system, this study considers China as the study area and investigates the monthly data of temperature (T) and precipitation (P) during 1900–2020 that were obtained from 3836 grid stations. The strong interaction and lag distribution between T or P with SA and CO were studied and influence weights of SA, CO, and geographical factors (GF) of each grid station were calculated. A multivariate hysteretic decomposition model was established to simulate and quantitatively decompose the periodic lag considering the factors of the earth’s revolution. The results indicate the existence of two dividing lines in the distribution of T and P lag periods. Additionally, the underlying surface conditions and urbanisation were observed to have significant effects on the periodic lag of meteorological elements.

1 **Spatiotemporal Hysteresis Distribution and Decomposition of Solar Activities and**
2 **Climatic Oscillation during 1900–2020**

3
4 Mingyang Li¹, Tingxi Liu^{1,*}, Long Ma^{1,*}, Limin Duan¹, Yixuan Wang¹, Guoqiang Wang², Huimin Lei³, Vijay Singh⁴

5
6 ¹ Inner Mongolia Water Resource Protection and Utilization Key Laboratory; Water
7 Conservancy and Civil Engineering College, Inner Mongolia Agricultural University, Hohhot
8 010018, China;

9 ² College of Water Sciences, Beijing Normal University, Beijing 100875, China;

10 ³ State Key Laboratory of Hydrosience and Engineering, Department of Hydraulic Engineering,
11 Tsinghua University, Beijing 100084, China;

12 ⁴ Department of Biological and Agricultural Engineering & Zachry Department of Civil
13 Engineering, Texas A& M University, College Station, TX 77843, USA).

14
15 Corresponding author: Tingxi Liu (txliu1966@163.com)

16 Long Ma (838276345@qq.com)

17 **Key Points:**

- 18 • Two distinct dividing lines in the hysteresis distribution of T and P respectively
19 • MHDMM descript how lag of SA to T & P decomposed into CO, SY & GF
20 • Weight distribution of SA, GF and CO in RGB false color synthesis
21

22 **Abstract**

23 Meteorological elements have different lag periods for solar activities (SA), climatic oscillation
24 (CO) and other influencing factors at different spatiotemporal scales. To further understand the
25 "solar-climate-water resource" system, this study considers China as the study area and
26 investigates the monthly data of temperature (T) and precipitation (P) during 1900–2020 that were
27 obtained from 3836 grid stations. The strong interaction and lag distribution between T or P with
28 SA and CO were studied and influence weights of SA, CO, and geographical factors (GF) of each
29 grid station were calculated. A multivariate hysteretic decomposition model was established to
30 simulate and quantitatively decompose the periodic lag considering the factors of the earth's
31 revolution. The results indicate the existence of two dividing lines in the distribution of T and P
32 lag periods. Additionally, the underlying surface conditions and urbanisation were observed to
33 have significant effects on the periodic lag of meteorological elements.

34 **1 Introduction**

35 Air temperature (T) and precipitation (P) are the primary indicators reflecting the climatic
36 characteristics of a region and the key factors influencing the ecohydrological cycle and balanced
37 exchange of water and heat (Chen et al., 2021b; Li et al., 2020; Song and Wu, 2021). Both T and
38 P exhibited relatively unique variation and distribution patterns in different spatiotemporal scales
39 (Zhang, 2021). They display distinct periodic characteristics due to astronomical and terrestrial
40 factors such as solar activities (SA), planetary positions of the sun and earth, climatic oscillation
41 of the earth (CO) and zonal characteristics due to geographical factors (GF) such as latitude and
42 longitude, terrain level, and underlying surface properties (Chen et al., 2021a; Nan et al., 2021;
43 Wood et al., 2020). The processes and mechanisms of different influencing factors on individual
44 components of hydrothermal balance vary; this variation causes different lag periods in the
45 responses of T and P in different regions (Huang et al., 2020; Yetemen et al., 2019). The coupling
46 effect of numerous factors requires thorough investigation to enable better understanding of the
47 "sun-earth climate-water resource" system, quantitative simulation and calculation of the coupling
48 relationships of components, accurate prediction of extreme climatic changes. Additionally,
49 understanding the factors and their effects can also help in ensuring improved and rapid responses
50 to climatic changes.

51 SA refers to various active phenomena in local areas of the solar atmosphere, primarily
52 caused by electromagnetic processes in the solar atmosphere (Friis-Christensen and Lassen, 1991).
53 These phenomena include occurrence of sunspots, light spots, spectral spots, flares, prominences,
54 and activities in the corona. SA has an average cycle of 11.2 a (Wilcox, 1976) and has been
55 associated with earthquakes, volcanic eruptions, droughts, floods, and even diseases of the human
56 cardiac and nervous systems (Marchitelli et al., 2020). Sunspot numbers (SN) are caused by strong
57 magnetic field activity of the sun that inhibit convection, cooling the surface and giving an
58 appearance of a relatively darker colour to the region, which are the most common and prominent
59 of all SAs.

60 The effects of SN on the Earth's climate garnered increasing interest in the early 20th
61 century. However, the investigations had certain limitations; some focused on a single site, such
62 limitations prevented a comprehensive understanding of the effects of SN, while others had a short
63 study duration. Since the 1990s, relevant studies have improved on spatiotemporal scales; however,
64 the accuracy of the surface scale studies and regional representation remain poor. Investigations
65 are primarily stagnated at the macro discussion and comparison levels (Friis-Christensen and

66 Lassen, 1991; Haigh, 1996). With the frequent occurrence of extreme weather events, studies after
67 the 21st century have become more extensive in both quantity and content (Brehm et al., 2021; De
68 la Torre et al., 2007; Li et al., 2018b; Ramanathan et al., 2001; Ramanathan and Feng, 2009; Xu
69 et al., 2021). According to the aforementioned studies, SN, as an important indicator representing
70 SA, can explain the hysteresis effect of T and P. However, due to the partial consideration of
71 factors, the results of these studies are limited to the fixed law of the lag period, such as the change
72 of the position relationship between the sun and the earth caused by the revolution of the earth,
73 CO; other key elements are not included in the model or analysis.

74 CO refers to a statistically significant change or long-term change in climate state due to
75 natural or anthropogenic factors, which reflects the climatic state of small regions and small basins,
76 and is affected by SA and other aspects (Nishikawa et al., 2021). Southern Oscillation Index (SOI)
77 and Sea Surface Temperature (SST) are two important indicators reflecting CO (Abtew et al., 2009;
78 Namadi and Deng, 2021). Both represent the interaction and equilibrium process of the
79 atmospheric and oceanic coupling system and can more carefully describe the abnormal
80 phenomena such as El Niño, La Niña and El Niño (Du et al., 2020; Kamruzzaman et al., 2020;
81 Kang et al., 2019). Existing studies that have investigated the influence of CO on regional T or P
82 space focused on the spatial distribution law, instead of the distribution law of lag, and the studies
83 considering SA and CO are even less rare. In terms of the specific influencing factors, most of
84 studies have explored the influence or lag effect qualitatively through the statistical law; however,
85 only a few studies established mathematical or mechanism model for quantitative research.
86 Moreover, most of studies are conducted on a small scale in terms of regional selection and few
87 cross-climatic zones (Dikshit et al., 2021).

88 This study used the data of raster weather stations in China collected during 1900–2020
89 and the data of SA and CO in long-time series (Figure 1). The time series law and spatial
90 distribution characteristics of all indicators under long-time series were investigated. The periodic
91 and hysteresis effects of SA and CO on T and P of China were analysed under six periodic scales.
92 Based on the comprehensive consideration of the earth's revolution process, a multivariate
93 hysteresis decomposition (MHD) model was proposed and established. We regrouped the study
94 area according to the weight of influential factors, quantitatively decomposed the contribution of
95 factors affecting the lag of T and P, and simulated the lag period.

96 **Figure 1** Schematic diagram of regional temperature and precipitation under the combined
97 influence of solar activity and climatic oscillation.

98 **2 Materials and Methods**

99 **2.1 Study area**

100 The research area corresponds to the People's Republic of China (73°33' -135°05' E, 3°51'
101 -53°33' N), located in the east of Asia and the west coast of the Pacific Ocean. The overall terrain
102 is high in the west and low in the east, with a ladder distribution and a vast area of mountains and
103 plateaus. China can be divided into the northern region, the southern region, and the Qinghai–Tibet
104 Plateau region according to the 400 mm annual isohyet and the boundary line of the first and
105 second terrains. The overall monsoon climate is significant. During the same period of rain and
106 heat, the southern region is dominated by subtropical and tropical monsoon climates, the northern
107 region is dominated by temperate monsoon and continental climate, and the Qinghai–Tibet Plateau

108 region presents plateau mountain climate (Supplementary Figure S1). The research area and the
109 network of $0.5 \times 0.5^\circ$ raster weather stations used are shown in Figure 2.

110 **Figure 2** Map of the study region indicating the locations of the 3836 monthly global grid high-
111 resolution stations.

112 2.2 Method and model

113 This study divides the research period into six periodic scales, namely, short (0–5 and 5–
114 10 a), medium (10–30 and 30–60 a), and long (60–90 and 90–120 a), based on the overall analysis
115 of time series rule. The T and P data from 3836 grid meteorological stations across China were
116 used to study the cross and SN, SOI, and SST influence and lag time and space distribution analysis;
117 the results were combined with the site location, lag effect, and revolution of the earth to establish
118 an MHD model, dismantling and quantify various time scales in China's T and P a lag effect
119 mechanism (Figure 3).

120 **Figure 3.** Flowchart showing the derivation of datasets from the data on daily T, P, SN, SOI, and
121 SST, and their interaction mechanism. SN: sunspot number; SOI: southern oscillation index;
122 SST: NINO 3.4 sea surface temperature.

123 2.2.1 Regulation and cross influence analysis

124 Discrete Fourier Transform (DFT) is used to transform time series from time to frequency
125 domain for T and P, SN, SOI, and SST data; then, the data structure and variation regulation of
126 time series were studied. The cross influence of T and P monthly data of 3836 grid meteorological
127 stations, spatiotemporal distribution analysis of SN, SOI, and SST, and lag were calculated using
128 the cross-wavelet transform (Taghizadeh-Mehrjardi et al., 2021) and the wavelet type was Morlet.
129 Within the 95% confidence interval of the six periodic scales, we extracted the period represented
130 by the most intense value of power from the wavelet power spectrum and the condensed spectrum
131 respectively as the period of interaction or lag between the station and the corresponding elements.
132 In the spatial and temporal distribution of strong interaction and lag period, if there are multiple
133 peaks in the series of temporal numbers under a time scale, we consider the maximum value as the
134 result of the station under this periodic scale. In the calculation of the lag period, 1/2 of the periodic
135 scale is taken as the zero point, the co-direction phase relation is taken as positive, and the reverse
136 phase relation is taken as negative. In order to facilitate the mapping and analysis of the lag
137 distribution, the reverse phase relation is rotated 1/2 of the period to be taken as positive. Under a
138 large periodic scale, there will be a long pseudo-lag (pseudo-interaction) period, which we call
139 superimposed lag (interaction) period.

140 2.2.2 Regulation and cross influence analysis

141 The variation of time series of meteorological elements is affected by long-term trends,
142 seasonal, and irregular variations. To eliminate random factors in the data, we used seasonal-trend
143 decomposition based on loess (STL) to smooth the data (Figure 4a, b). The STL method is a time
144 series decomposition method with both generality and robustness. It is characterised by self-
145 control of trend, smoothness of periodic components, and good robustness to outliers.

146 There is an auto cross correlation of a meteorological element and itself at different time
147 points. We used autocorrelation function to conduct autocorrelation analysis on T and P data of

148 each grid meteorological stations. The time delay coefficient is obtained through the self-
 149 covariance, namely, the self-delay period of this element (SY), which can be used for the
 150 subsequent quantitative separation of elements in the MDH model (Figure 4c, d).

151 **Figure 4.** The original, seasonal, trend and residual terms of T (a) and P (b) by seasonal and trend
 152 decomposition using loess method (STL) and the autocorrelation using the residual terms of T (c)
 153 and P (d) by STL. Graph shows the data preprocessing of the sample grid station of China, and
 154 this method is applied to all station data used in the study.

155 2.2.3 MDH model

156 In order to explore the interaction relationship and mutual feed mechanism among
 157 meteorological elements in the SA-CO region, based on the hysteresis period of T and P of each
 158 grid station, we decomposed the hysteresis period of SA on meteorological elements into the
 159 influence of SA on CO, as well as the transformation of CO, GF, including longitude, latitude, and
 160 elevation), solar altitude angle (SEA for short, θ in model) caused by the revolution of the earth
 161 and meteorological element SY. The aforementioned decomposition factor relations is expressed
 162 in Figure 3 and Eq. 1.

$$163 \quad A = \alpha_1 A' + f(B, C) + g(\text{Lat}, \text{Lon}, \text{Alt}) + \alpha_2 D + \delta \quad (1)$$

$$164 \quad f(B, C) = \tau_1 B \times \tan\theta + \tau_2 C_1 + \tau_3 C_2 \quad (2)$$

$$165 \quad g(\text{Lat}, \text{Lon}, \text{Alt}) = \rho_1 \text{Lat} + \rho_2 \text{Lon} + \rho_3 \text{Alt} \quad (3)$$

166 where, A, B, C, D represent the hysteresis period of the SA to meteorological elements, the
 167 solar to climate, the CO to local meteorology and the SY period of meteorological factors,
 168 respectively. A' is the strong action of SA on meteorological elements. C can be divided into C_1
 169 and C_2 , which respectively represent the period of hysteresis effect and strong action of SA on CO.
 170 θ is SEA. $\alpha_1, \alpha_2, \alpha_3$ are the hysteresis adjustment coefficient of the earth's climate, GF, and SY,
 171 respectively; τ_1, τ_2, τ_3 are the influence parameters of the SA on the climate and the CO on local
 172 meteorological conditions; ρ_1, ρ_2, ρ_3 are the hysteresis response parameters of GF (latitude,
 173 longitude, and elevation) to meteorological elements, respectively; δ is the regulating parameter
 174 of the solar - CO - local meteorological hysteresis model.

175 During the earth's revolution, the angle of incidence of sun's rays on the earth changes,
 176 which determines the amount of solar heat received by the earth surface. The SEA at the locations
 177 of grid meteorological stations in the study area is used to represent the influence of the earth at
 178 different positions in the orbit, which can be calculated by Eq. 4.

179 The SEA varies with local time, local latitude, and the sun declination, and can be
 180 expressed as:

$$181 \quad \sin\theta = \sin\sigma \times \sin\varphi + \cos\sigma \times \cos\varphi \times \cos t \quad (4)$$

182 where, the declination of the sun (latitude equal to the point of direct sunlight) is expressed
 183 by σ ; the geographic latitude of the observation site is expressed by φ (both solar declination and
 184 geographic latitude are positive in the north latitude and negative in the south latitude); and the
 185 local time (hour angle) is expressed by t .

186 2.2.4 Entropy weights method

187 Entropy is a measure of the disorder of a system. According to the definition of information
 188 entropy, for a certain index, the entropy value can be used to judge the degree of dispersion of an
 189 index. The smaller the information entropy value is, the greater the degree of dispersion of the
 190 index will be, and the greater the influence (i.e. weight) of the index on the comprehensive
 191 evaluation will be. If all the values of an index are equal, the index has no effect in the
 192 comprehensive evaluation. Therefore, the tool of information entropy can be used to calculate the
 193 weight of each index and provide a basis for the comprehensive evaluation of multiple indexes.
 194 We standardized the data of each index. Given k indices X_1, X_2, \dots, X_k , where

$$195 X_i = \{x_1, x_2, \dots, x_n\} \quad (5)$$

196 Assume that the normalized value of all index data are $\{Y_1, Y_2, \dots, Y_n\}$. We can get

$$197 Y_{ij} = \frac{x_{ij} - \min(X_i)}{\max(X_i) - \min(X_i)} \quad (6)$$

198 The information entropy of a set of data can be defined as:

$$199 E_j = -\frac{1}{\ln n} \sum_{i=1}^n p_{ij} \ln p_{ij} \quad (7)$$

200 where, $p_{ij} = Y_{ij} / \sum_{i=1}^n Y_{ij}$. If $p_{ij} = 0$, we define $\lim_{p_{ij} \rightarrow 0} p_{ij} \ln p_{ij} = 0$. According to the calculation
 201 formula of information entropy, the information entropy of each index is calculated as
 202 $\{E_1, E_2, \dots, E_n\}$. The weight of each index is calculated by information entropy:

$$203 W_i = \frac{1 - E_j}{k - \sum E_i} \quad (i = 1, 2, \dots, k) \quad (8)$$

204 2.2.5 Hysteresis area grouping and model evaluation index

205 K-means clustering, which is popular for cluster analysis in data mining, aims to partition
 206 n observations into K -clusters in which each observation belongs to the cluster with the nearest
 207 mean, serving as a prototype of the cluster. At each grid station, the influence entropy weights of
 208 SA, CO and GF are grouped into 6 groups, which respectively represent the scenario in which the
 209 two of the three influence factors have the highest weight ratio.

210 p values were used to test the sample variance of the measured and the simulated values,
 211 and the significance level was set to 0.05. When the p value was less than 0.01, there was a highly
 212 significant statistical difference. We use the coefficient of determination (R^2) and the root-mean-
 213 square error (RMSE) to evaluate the lag (superimposed lag) period of MDH model simulation.
 214 They are defined as follows:

$$215 R^2 = 1 - \frac{RSS}{TSS} \quad (9)$$

$$216 RMSE = \sqrt{\frac{\sum_{t=1}^n (I_p - I_o)^2}{n}} \quad (10)$$

217 where RSS is the residual sum of squares; TSS is the total sum of squares; I_p and I_o are the
 218 observed and predicted lag (superimposed lag) period (a), respectively; and n is the total simulation
 219 number.

220 3 Data

221 The research data includes the monthly T and P data of 3836 raster weather stations from
 222 1900 to 2020, the index SN of SA, the monitoring index SOI and Nino 3.4 SST of CO, and the
 223 digital elevation model (DEM) of the location of the raster weather stations in the research area
 224 (Table 1). Among them, “Udel_ airt_precip” data is used for data from 1900 to 2017 (Willmott and
 225 Matsuura, 2001), and data interpolation from China’s national meteorological stations is used for
 226 data from 2018 to 2020.

227 **Table 1.** Utilized information and number of T, N, SN, SOI, SST, SEA and DEM data in the
 228 research. T: air temperature; P: precipitation; SN: sunspot number; SOI: southern oscillation index;
 229 SST: NINO 3.4 sea surface temperature; SEA: solar elevation angle; DEM: digital elevation model.

230 4 Results

231 4.1 Periodic distribution of T and P

232 The periodic distribution of T in China at the scale of 0–5 a is similar to that in climatic
 233 zones. T has a significant period of 6–8 a between 25° N and 45° N on the scale of 5–10 a. On the
 234 scale of 10–30 a, the significant period of T increased step-by-step from east to west, and increases
 235 in the region to the west of 80° E (Figure 5a).

236 Compared with T, the periodic distribution of P is more scattered and patchier, which is
 237 mainly manifested in the 2–4 a period of the central and eastern part of China at the scale of 0–5
 238 a, and the 1 a period of the Qinghai–Tibet region in the northwest of China. At 5–30 a scale, the
 239 significant period of P in Northeast, North, and East China was approximately 8–14 a. The P
 240 significant period in the northwest of Mount Qomolangma at the 5–90 a scale slightly varies from
 241 that in the Qinghai–Tibet region, and it mainly exhibits significant periods at 7.5, 34 and 88 a
 242 (Figure 5b). The obtained results are consistent with the results of Sun et al. (2017) that were
 243 obtained using the national meteorological stations data in China to study the spatial heterogeneity
 244 and annual distribution of T and P.

245 **Figure 5.** Grided, latitude and longitude scale distribution of (a) T and (b) P periodicity of China
 246 under six periodic scales (1900–2020).

247 4.2 Periodic distribution of T and P

248 In terms of periodicity, SN is extremely active during 7.3–16.1 a, with an average cycle
 249 length of 11.2 a. There is a century cycle of SA in 80–90 a, with 3 or 4 consecutive 11.2 a
 250 significant peaks followed by 3 or 4 consecutive 11.2 a low peaks (Figure 6a). The most significant
 251 regulation of SOI sequence is 1 a; the 2.5 a cycle is also significant (Figure 6b). A substantial
 252 proportion of the energy fluctuations of SST in Nino3.4 region were primarily distributed in the
 253 period 1 a and 2–7 a. There is a significant period of 9–14 years from 1970 to 2015 (Figure 6c).
 254 According to the cross-wavelet analysis of SN, SOI, and SST (Figure 6d–g), a significant
 255 interaction between SA and CO mainly occurs in the periods of 0.25, 0.5, 1 a and 8–16 a.

256 **Figure 6.** Continuous wavelet spectra of SN, SOI and SST (a–c). Cross wavelet transforms and
 257 wavelet coherences between SN and SOI (d, f), SST (e, g). (The thin solid line represents the
 258 wavelet influence cone, the thick solid line represents the horizontal interval of 5 % significance,

259 the right arrow represents the concentric phase relationship, and the left arrow represents the
260 inverse phase relationship.)

261 4.3 Interaction period distribution

262 The periodic distribution of strong interaction between SN, T, and P was consistent with
263 significant high correlation periods of 1.03, 11.02 and 83.21 a. The significant superposition
264 interaction periods were 9.82, 55.53 and 88.15 a. On the scale of 10–30 a, T in northern China
265 exhibited a significant high correlation period of 9.82 years. Furthermore, on the 0–5 a scale, the
266 precipitation in some areas of Northwest China displayed a significant high correlation period of
267 4.63 a (Supplementary Figure S2a, b; Supplementary Table S1).

268 The strong interaction periods of SOI and Nino3.4 SST against T and P were consistent
269 with those observed in the study area. The results indicated periods of significant high correlation
270 between CO and T at 1.03, 11.02 and 83.21 a. The significant superposition interaction periods
271 were 9.27, 9.82, 55.53, 58.84 and 88.15 a. On the 10–30 a scale, the strong interaction period of T
272 in the northwest, southwest and north of China was relatively large. On the 60–90 a scale, the
273 strong interaction period of T in Northeast China and South China was relatively small. The strong
274 interaction period of P was relatively high in the 10–30 a scale in Northeast China (Supplementary
275 Table S2).

276 Compared with T, the strong interaction period distribution of CO and P indicated patchier
277 characteristic, and the second significant high correlation periods were primarily 1.09, 2.45
278 (Southeast and Northwest China), 11.67, 24.73 (Northeast China and along the Kunlun Mountains),
279 44.07 (Central and South China), 58.84 a (patch distribution), etc. (Supplementary Figure S2c–f).

280 4.4 Hysteresis period distribution

281 Overall, the periodic hysteresis characteristics of T to SN and CO were concentrated at 0–
282 5 a and 60–120 a scales in spatial distribution, whereas the patchiness of P was more significant.
283 The main lag response periods of T to SA were 0.24–0.63, 1.03–3.58, and 4.55–10.78 a
284 (Supplementary Table S3); the superimposed lag periods included 21.34–24.84, 57.79–65.11, and
285 66.28–69.91 a (Figure 7a). Additionally, on the 0–5 a scale, the lag period in eastern region was
286 slightly longer than that of the western region by 0.1–0.2 a. On the 5–10 a scale, the hysteretic
287 response period of North China, East China and Central China was slightly shorter, ranging from
288 0.57 to 1.29 a. On the scale of 60–120 a, the superimposed hysteresis period of Tarim Basin,
289 Tanggula Mountain and Sichuan Basin was significant.

290 The primary lag response periods of T to CO were 0.25–0.54, 1.39–4.08, and 6.25–7.25 a
291 (Supplementary Table S4); the superimposed lag periods included 9.74–12.82, 24.91–29.36,
292 56.27–61.89, and 65.78–69.64 a (Figure 7c, e). Moreover, on the 5–10 a scale, the hysteretic
293 response period of Northwest, Northeast, and East China was slightly shorter. On the scale of 10–
294 30 a, the P hysteresis response period in the eastern region was longer. On the 60–120 a scale,
295 there were two distinct superimposed hysteresis dividing lines in the east and west respectively:
296 the Central Gobi–Ordos Plateau–Hengshan–Yanshan Mountains, and the southern foot of the
297 northern Tibetan Plateau–Chechen River–Turpan Basin.

298 The main hysteresis response cycles of P to SN were 0.25–0.54, 1.39–4.08, and 5.20–7.10
299 a (Supplementary Table S3); the superimposed hysteresis cycles included 11.91–18.72, 21.85–
300 25.36, and 48.99–59.43 a (Figure 7b). On the 10–30 a scale, the hysteresis period of North China

301 and Northern Central China was slightly longer. On the 30–60 a scale, the hysteresis period of
302 northeast, southeast and western regions was relatively short, which is 30.87–37.87 a. The main
303 lag response period of P to CO was similar to that of T, but the distribution characteristics were
304 different (Figure 7d, f). On the 5–10 a scale, the hysteresis period of Northeast China and Sichuan
305 Basin was relatively short. On the 10–30 a scale, the superimposed hysteresis period of Northeast
306 China and the eastern part of the Qinghai–Tibet Plateau was slightly longer. On the scale of 60–
307 120 a, P also contained two distinct superimposed hysteresis cycle dividing lines: The Greater
308 Hinggan–Taihang–Wushan–Xuefeng Mountains and the Qilian–Bayankla–Hengduan
309 Mountains.

310 **Figure 7.** The significant lag period distributions of SN (a, b), SOI (c, d) and SST (e, f) to T and
311 P of China under six periodic scales (The significance level = 0.95).

312 4.5 Analysis of influencing factors

313 To further study the effects of SA, CO, and GF on the T and P periodic hysteresis in China,
314 the entropy weight method was employed to analyse the contribution weight of the hysteresis
315 effect of grid stations over 121 years. We used false colour synthesis to facilitate observation. The
316 influence weight of SA corresponds to the intensity of red in the RGB channel, whereas CO and
317 GF correspond to blue and green respectively (Figure 8). The results indicated that the weights of
318 periodic lag factors of T and P have distinct geographical boundaries that are consistent with the
319 boundaries of lag effects of T and P at the scale of 60–120 a.

320 GF is an important factor affecting the lag of T and P in China. The periodic lag of T is
321 significantly affected by SA and CO in Northeast, Northern North, and Western Northwest China.
322 The periodic lag of P is highly affected by SA and CO in the central and northern regions of China;
323 furthermore, it is highly affected by SA and GF in the Sichuan basin and the upstream region of
324 the Yellow River.

325 **Figure 8.** Entropy weight of SA, CO, and regional GF to the periodic hysteresis of T (a) and P
326 (b) under six periodic scales in China. Red, blue, and green represent SA, CO, and GF,
327 respectively (significance level = 0.95).

328 4.6 Geographical partition of influencing factors

329 Clustering k-means was used to divide 3836 grid meteorological stations in the research
330 area into six groups according to the influence weights of SA, CO, and GF on the T and P periodic
331 lag in China. These groups corresponded to the arrangement and combination of the weights of
332 the three influencing factors (Supplementary Figure S3), to facilitate the decomposition of MHD
333 model and the simulation of the lag effect of meteorological elements. The results demonstrated
334 that the weight clustering partition retained the delay effect boundary. The western and
335 northeastern mountains of China form their own groups in the lagged grouping of T. The Northeast
336 Plain and the Inner Mongolia Plateau were combined into a group, similar to the grouping used
337 for the Loess Plateau, Sichuan Basin and Yunnan–Guizhou Plateau. The lag group of P was similar
338 to the terrain trend. The northeast plain and surrounding mountains were divided into two groups,
339 while the eastern coastal plain and mountain areas were separated.

340 4.7 Quantitative simulation of lag effects

341 The strong interaction period, lag effect period and solar altitude angle (SEA) of the six
 342 periodic scales generated above were respectively substituted into MHD model in groups
 343 according to the weights of the six influencing factors to simulate the lag period of the study area
 344 under different periodic scales. The model parameters and accuracy error analysis are detailed in
 345 Supplementary Table S5 and Figure 9. The results indicated that the overall effect of MHD model
 346 in splitting and simulating the T hysteresis effect was better than that of P. For regions below 40°
 347 N, the T lag simulation R^2 of the model was between 0.6–0.95. The interpretation degree was not
 348 high in Northeast and North China, and several regions with error values >10 a were scattered in
 349 Northwest and Southwest China. The accuracy and error of P lag simulations in East, South, and
 350 South-Central China were excellent; although, the simulation error in North China was low, the
 351 interpretation degree was not high. The model had a high degree of interpretation for the Himalayas,
 352 Qinghai Lake, and southern Taiwan province, but the error of the six periods was large (Figure 9).

353 **Figure 9.** Accuracy (a, b) and error (c, d) analysis of simulated T (a, c) and P (b, d) hysteresis
 354 period distribution using multivariate hysteretic decomposition model (MHD model; Eq.1).
 355 RMSE: root mean squared error (The significance level = 0.95).

356 5 Discussion

357 5.1 Hysteretic response mechanism and pseudo-cycle

358 According to the fluctuation characteristics of meteorological elements, SA, and CO in the
 359 same time domain, it was observed that T and P have the same variation period in multiple time-
 360 frequency domains (Huang et al., 2020; Li et al., 2018a; Yetemen et al., 2019). In addition to the
 361 interannual period (1.03 a), the interaction between T and P and SN and CO was prominently
 362 strong at the SA and Glasberg periods of 9–13 a (average 11.2 a) and 80–90 a (average 87 a),
 363 respectively. There was also a strong interaction between the middle part of the research area and
 364 CO with a 21–25 a Haier cycle (average 22 a) (Supplementary Figure S2). The hysteresis response
 365 cycles are more abundant in spatiotemporal scales. The hysteresis (superposition hysteresis) cycles
 366 included interannual, SA, and Haier cycles; moreover, they were significant in 3–6 and 64–70 a
 367 cycles.

368 Although, both T and P have hysteresis effect on the fluctuation of SA and CO in the long-
 369 time scale, it was observed that in the same region, long interaction/hysteresis period can be
 370 obtained by combining short interaction/hysteresis period with the length of SA period. For
 371 example, under the interaction period of 90–120 a, the significant period of 88.15 a can be perfectly
 372 decomposed into 4 11.02 a (Supplementary Table S1, S2). The superimposed significant lag period
 373 of precipitation at the scale of 60–90 a is a multiple of the sum of two small significant lag periods
 374 at the scale of 0–5 and 5–10 a (Supplementary Figure S4). Even the lag close to the SA cycle can
 375 be decomposed into 2–3 significant lag cycles at the 5–10 a scale (Supplementary Table S3, S4).
 376 Previous studies suggest that the spatial lag of meteorological elements can be understood as the
 377 combined result of many individual event responses (Kamruzzaman et al., 2020; Namadi and Deng,
 378 2021) and illustrate the importance of identifying true and false cycles in studying
 379 interaction/hysteresis processes.

380 5.2 Analysis of interaction lag distribution and influence effect

381 For a long periodic scale (60–120 a), the periodic correlation distribution of SN and CO to
 382 T or P is the same in the entire study area. The results suggest that the effects of SA and CO on T
 383 or P have mutual effects of assimilation across topographical and climatic zones, and the
 384 assimilation can be understood as the geographical homogenisation of climatic elements. The
 385 strong interaction distribution results indicate that SOI and Nino3.4 SST have the same influence
 386 on the lag period distribution of regional T and P, suggesting that the influence of CO on regional
 387 meteorological elements, introduces consistency in the CO index in the region (van der Kaars et
 388 al., 2010).

389 The distribution pattern of strong interaction and lag periods exhibited distinct
 390 geographical division at various scales, and the regional boundaries of different intensities and
 391 periods were approximately consistent with the intense fluctuation of terrain. The lag periods of T
 392 and P and the dividing line of the pattern of influencing factors can be divided into the east line
 393 and the west line, both of which are reflected in the strong interaction and periodic lag response.
 394 The T lag dividing lines run through water veins or valleys where mountains meet, and the gaps
 395 in the mountains facilitate the cross-regional flow of monsoons. The P lag dividing lines are the
 396 zones of drastic terrain change, where the high mountains block the transport of water vapour.
 397 Considering the average lag period of seven regions in China for comparison, it was found that the
 398 northern region of China has the longest lag period, and the lag period of surrounding regions tends
 399 to converge to the northern region. The lag period caused by SN in Southwest China is greater
 400 than that in Northwest China, while the lag effect of CO is opposite for the aforementioned two
 401 regions (Figure 10a-b). The lagging trend of precipitation also has similar characteristics, except
 402 that the central part of China has the longest lag period (Figure 10c-d).

403 **Figure 10.** Theoretical diagram of the variation of (a, b) T and (c, d) P on the hysteresis period
 404 distribution of (a, c) SN and (b, d) CO. NW: Northwest China; N: North China; SW: Southwest
 405 China; E: Eastern China; C: Central China; S: South China.

406 The lag spatial distribution of T and P shows that it is nested with the terrain (Brunner et
 407 al., 2021) and echoes with the city (Marelle et al., 2020). Additionally, abrupt topographical
 408 changes within distinct boundaries, such as those in the Tarim Basin in western China also affect
 409 the lag spatial distribution. Based on the hysteresis effect on T, it can be deduced that the northern
 410 Tarim Basin is the region where GF has great influence. For P, SA has a significant effect on the
 411 Taklimakan Desert, south of Tarim Basin.

412 Regional underlying surface conditions and anthropogenic activities are also important
 413 factors affecting T and P periodic lag (Wood et al., 2020), which is particularly reflected in the
 414 patchy distribution of P period lag. According to the weighting factors of the influence of P in the
 415 decomposition, there are two dominant area that are mainly affected by SA and GF (Figure 5b
 416 slant yellow area), are primarily distributed in the Loess Plateau, the northeast and the Yunnan–
 417 Guizhou plateau, Maowusu sandy land; the areas respectively correspond to the two major rivers,
 418 the bend of Yellow River and the middle and upper reaches of Yangtze river (Yibin–Three gorges).
 419 In this instance, GF can provide more information on underlying surface (Brunner et al., 2021;
 420 Wei et al., 2021). The patchy lag distribution of P is also significantly related to anthropogenic
 421 activities such as urbanisation (Marelle et al., 2020; Zhang et al., 2021).

5.3 Hysteresis decomposition and uncertainty analysis

From the simulation results, it can be understood that there remains a substantial scope for improvement in the disassembly and simulation of hysteresis effect (Figure 9). According to the obtained results, urbanisation has a significant impact on the periodic lag distribution of P. In this study, the weights of three influencing factors, SA, CO, and GF, were classified and clustered, which met the zoning requirements of surface scale (Michniewicz et al., 2020). However, for P, a meteorological element with conspicuous patchiness, it was targeted to a greater extent at the group level by adding urbanisation level indicators (Marelle et al., 2020), such as proportion of land for construction and urbanisation level, which may substantially improve the control of P characteristics (Du et al. 2020).

Furthermore, the consideration of influencing factors and method of decomposition of factors increase the uncertainty levels in the study. Influencing factors of the uncertainty of both celestial, space weather (such as the gravitational pull of the moon and interference of the interplanetary magnetic field) may affect the propagation process of solar energy in space (Zheng et al., 2019), including the earth itself (such as ocean currents and volcanic eruptions), and directly or indirectly alter the local climate (Marchitelli et al., 2020). The decomposition of the influencing factors can also be improved. Regardless of the scope of physical or semi-physical improvement in the connection between the components according to the influencing mechanism, a refined geographical division and larger spatiotemporal scale are conducive to the effective analysis of the hysteresis response of meteorological factors to SA and CO.

6 Conclusions

In this study, we investigated the periodicity of T and P in China over 121 years from 1900 to 2020 on six periodic scales. the strong interaction period with SA and CO and the hysteresis effect on them was also studied. The weight distribution of factors influencing T and P periodic hysteresis in China was plotted, and the hysteresis responses of T and P to SA, CO, and GF were quantified and simulated by MHD model.

The results indicate that T and P have a similar variation period in multiple time-frequency domains and a distinct strong interaction and lag or superposition lag period in interannual, SA, Haier, and Glassberg cycles. The long superposition interaction/hysteresis period can be divided into several short interaction/hysteresis periods. The periodic distribution of strong interaction and lag indicates that they are nested with the terrain and correspond with the city at a distance. Additionally, the underlying surface conditions and urbanisation are important factors affecting the periodic hysteresis of T and P. There are two distinct dividing lines in the lag period of T and P and the pattern of influencing factors, respectively. The dividing lines of T are between mountains and valley terrain, that include the Central Gobi–Ordos Plateau–Hengshan–Yanshan and the southern foot of the northern Tibetan Plateau–Cherchen River–Turpan Basin. The dividing lines of P correspond to the zone of sharp terrain change that include the Greater Hinggan—Taihang—Wushan–Xuefeng Mountains and Qilian—Bayankela–Hengdun Mountains.

Acknowledgments, Samples, and Data

This research was funded by the National Natural Science Foundation of China (Nos. 51939006 and 51620105003), the National Key R&D Program of China (No. 2018YFC0406400), the Inner

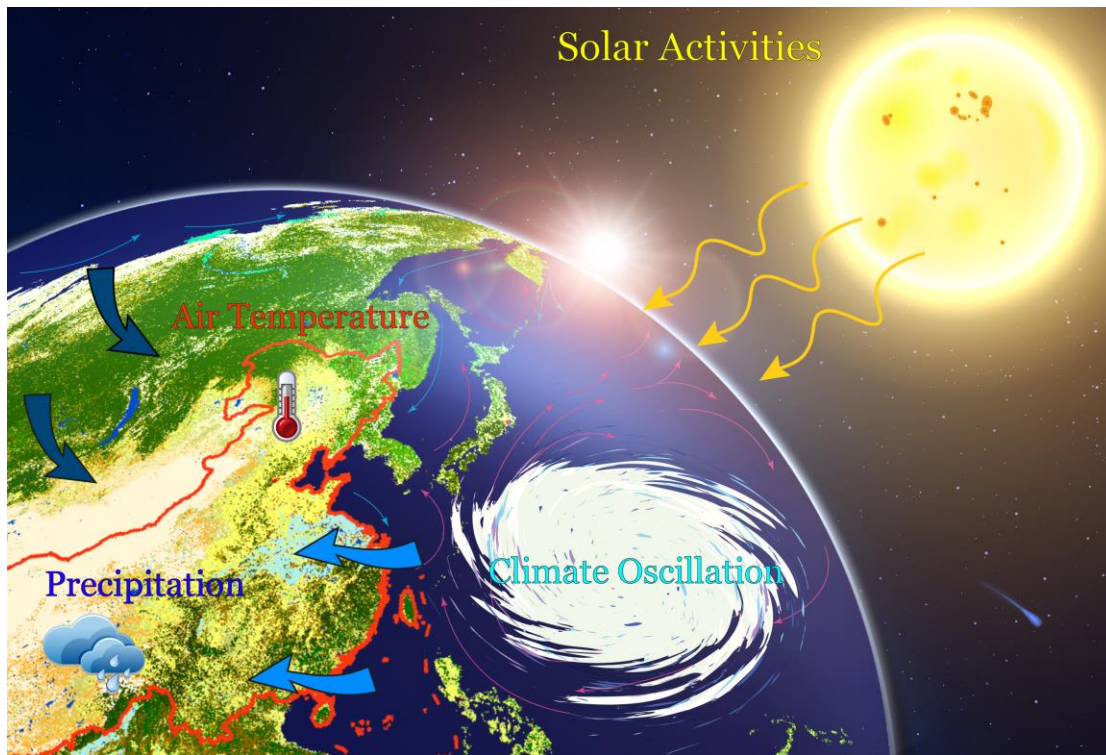
464 Mongolia Science and Technology Plan Project (No. 2020), the Ministry of Education Innovative
465 Research Team (No. IRT_17R60), the Inner Mongolia Industrial Innovative Research Team (No.
466 2012), the Natural Science Foundation of Inner Mongolia Autonomous Region of China (No.
467 2020JQ06), the Inner Mongolia Major science and technology projects (No. 2019ZD007). Thanks
468 for the UDel_AirT_Precip data provided by the NOAA/OAR/ESRL PSL, Boulder, Colorado, USA,
469 from their Web site at https://www.psl.noaa.gov/data/gridded/data.UDel_AirT_Precip.html.
470 Thanks for the cross wavelet and wavelet coherence software provided by A. Grinsted. (C) Aslak
471 Grinsted 2002-2014 <http://www.glaciology.net/wavelet-coherence>. Thanks for the Sunspot Index
472 and Long-term Solar Observations data belongs to the Royal Observatory of Belgium (hereinafter
473 "ROB"), from their Web site at <http://sidc.oma.be/silso/monthlyssnplot>. Thanks for the Southern
474 Oscillation Index (SOI) data belongs to the Bureau of Meteorology, from their Web site at
475 <http://www.bom.gov.au/climate/current/soi2.shtml>. All generated methods used in this study can
476 be downloaded from <https://github.com/myli1993/T-P-response-to-SA-CO>. And generated data
477 can be downloaded from <https://pan.baidu.com/s/101t-wgtWa31Pf85J-VXO3A> and the extract
478 code is TPSA. There are no conflicts of interest to declare.

479 **References**

- 480
481 Abteu W., Melesse A.M., Dessalegne T. (2009) El Nino Southern Oscillation link to the Blue Nile River Basin
482 hydrology. *Hydrological Processes* 23:3653-3660. DOI: 10.1002/hyp.7367.
- 483 Brehm N., Bayliss A., Christl M., Synal H.A., Adolphi F., Beer J., Kromer B., Muscheler R., Solanki S.K., Usoskin
484 I., Bleicher N., Bollhalder S., Tyers C., Wacker L. (2021) Eleven-year solar cycles over the last millennium
485 revealed by radiocarbon in tree rings. *Nature Geoscience* 14:10-+. DOI: 10.1038/s41561-020-00674-0.
- 486 Brunner M.I., Swain D.L., Gilleland E., Wood A.W. (2021) Increasing importance of temperature as a contributor to
487 the spatial extent of streamflow drought. *Environmental Research Letters* 16:10. DOI: 10.1088/1748-
488 9326/abd2f0.
- 489 Chen C., Chen Q.W., Li G., He M.N., Dong J.W., Yan H.L., Wang Z.Y., Duan Z. (2021a) A novel multi-source data
490 fusion method based on Bayesian inference for accurate estimation of chlorophyll-a concentration over
491 eutrophic lakes. *Environmental Modelling & Software* 141:12. DOI: 10.1016/j.envsoft.2021.105057.
- 492 Chen F.H., Duan Y.W., Hou J.Z. (2021b) An 88 ka temperature record from a subtropical lake on the southeastern
493 margin of the Tibetan Plateau (third pole): new insights and future perspectives. *Science Bulletin* 66:1056-
494 1057. DOI: 10.1016/j.scib.2021.02.031.
- 495 De la Torre L., Gimeno L., Anel J.A., Nieto R. (2007) The role of the solar cycle in the relationship between the, North
496 Atlantic Oscillation and Northern Hemisphere surface temperatures. *Advances in Atmospheric Sciences*
497 24:191-198. DOI: 10.1007/s00376-007-0191-x.
- 498 Dikshit A., Pradhan B., Alamri A.M. (2021) Long lead time drought forecasting using lagged climate variables and a
499 stacked long short-term memory model. *Science of the Total Environment* 755:12. DOI:
500 10.1016/j.scitotenv.2020.142638.
- 501 Du Y.H., Berndtsson R., An D., Zhang L.N., Yuan F.F., Hao Z.C. (2020) Integrated large-scale circulation impact on
502 rainy season precipitation in the source region of the Yangtze River. *International Journal of Climatology*
503 40:2285-2295. DOI: 10.1002/joc.6332.
- 504 Friis-Christensen E., Lassen K. (1991) Length of the solar cycle: an indicator of solar activity closely associated with
505 climate. *Science (New York, N.Y.)* 254:698-700. DOI: 10.1126/science.254.5032.698.
- 506 Haigh. (1996) The Impact of Solar Variability on Climate. *Science (New York, N.Y.)* 272:981-4. DOI:
507 10.1126/science.272.5264.981.
- 508 Huang X., Ma L., Liu T.X., Sun B.L., Zhou Y., Yang C., Qiao Z.X. (2020) Spatial and temporal variability of the
509 abrupt interannual temperature change and warming hiatus in China, 1951-2016. *Meteorological*
510 *Applications* 27:17. DOI: 10.1002/met.1911.
- 511 Kamruzzaman M., Metcalfe A., Beecham S. (2020) Modelling spatial and temporal rainfall and their relationship to
512 climatic indicators in South Australia. *Theoretical and Applied Climatology* 142:543-553. DOI:
513 10.1007/s00704-020-03314-0.
- 514 Kang N.Y., Kim D., Elsner J.B. (2019) The contribution of super typhoons to tropical cyclone activity in response to

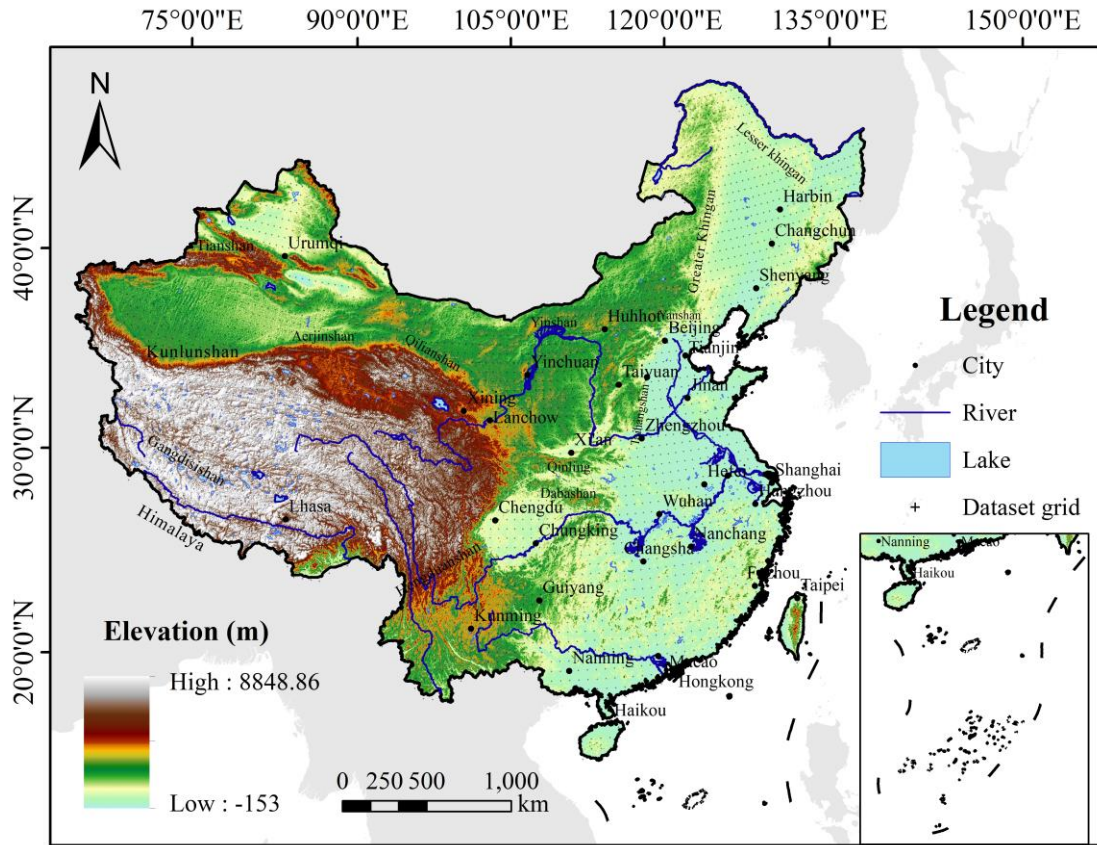
- 515 ENSO. *Scientific Reports* 9:6. DOI: 10.1038/s41598-019-41561-y.
- 516 Li M.K., Zhang S.Q., Wu L.X., Lin X.P., Chang P., Danabasoglu G., Wei Z.Q., Yu X.L., Hu H.Q., Ma X.H., Ma W.W.,
517 Jia D.N., Liu X., Zhao H.R., Mao K., Ma Y.W., Jiang Y.J., Wang X., Liu G.L., Chen Y.H. (2020) A high-
518 resolution Asia-Pacific regional coupled prediction system with dynamically downscaling coupled data
519 assimilation. *Science Bulletin* 65:1849-1858. DOI: 10.1016/j.scib.2020.07.022.
- 520 Li W., Duan L.M., Luo Y.Y., Liu T.X., Scharaw B. (2018a) Spatiotemporal Characteristics of Extreme Precipitation
521 Regimes in the Eastern Inland River Basin of Inner Mongolian Plateau, China. *Water* 10. DOI: ARTN 35
522 10.3390/w10010035.
- 523 Li Z., Yue J.P., Xiang Y.F., Chen J., Bian Y.K., Chen H.Q. (2018b) Multiresolution Analysis of the Relationship of
524 Solar Activity, Global Temperatures, and Global Warming. *Advances in Meteorology* 2018:8. DOI:
525 10.1155/2018/2078057.
- 526 Marchitelli V., Troise C., Harabaglia P., Valenzano B., De Natale G. (2020) On the Long Range Clustering of Global
527 Seismicity and its Correlation With Solar Activity: A New Perspective for Earthquake Forecasting. *Frontiers*
528 *in Earth Science* 8:8. DOI: 10.3389/feart.2020.595209.
- 529 Marelle L., Myhre G., Steensen B.M., Hodnebrog O., Alterskjaer K., Sillmann J. (2020) Urbanization in megacities
530 increases the frequency of extreme precipitation events far more than their intensity. *Environmental Research*
531 *Letters* 15:9. DOI: 10.1088/1748-9326/abcc8f.
- 532 Michniewicz A., Jancewicz K., Migon P. (2020) Large-scale geomorphological mapping of tors - Proposal of a key
533 and landform interpretation. *Geomorphology* 357:12. DOI: 10.1016/j.geomorph.2020.107106.
- 534 Namadi P., Deng Z.Q. (2021) Modeling and Forecasting *Vibrio Parahaemolyticus* Concentrations in Oysters. *Water*
535 *Research* 189:11. DOI: 10.1016/j.watres.2020.116638.
- 536 Nan S.L., Zhao P., Chen J.M., Liu G. (2021) Links between the thermal condition of the Tibetan Plateau in summer
537 and atmospheric circulation and climate anomalies over the Eurasian continent. *Atmospheric Research*
538 247:15. DOI: 10.1016/j.atmosres.2020.105212.
- 539 Nishikawa S., Wakamatsu T., Ishizaki H., Sakamoto K., Tanaka Y., Tsujino H., Yamanaka G., Kamachi M., Ishikawa
540 Y. (2021) Development of high-resolution future ocean regional projection datasets for coastal applications
541 in Japan. *Progress in Earth and Planetary Science* 8:22. DOI: 10.1186/s40645-020-00399-z.
- 542 Ramanathan V., Crutzen P.J., Kiehl J.T., Rosenfeld D. (2001) Aerosols, climate, and the hydrological cycle. *Science*
543 (New York, N.Y.) 294:2119-24. DOI: 10.1126/science.1064034.
- 544 Ramanathan V., Feng Y. (2009) Air pollution, greenhouse gases and climate change: Global and regional perspectives.
545 *Atmospheric Environment* 43:37-50. DOI: 10.1016/j.atmosenv.2008.09.063.
- 546 Song L., Wu R. (2021) Two Types of Rossby Wave Breaking Events and Their Influences on East Asian Winter
547 Temperature. *Journal of Geophysical Research-Atmospheres* 126. DOI: 10.1029/2020jd033917.
- 548 Taghizadeh-Mehrjardi R., Schmidt K., Toomanian N., Heung B., Behrens T., Mosavi A., Band S.S., Amirian-Chakan
549 A., Fathabadi A., Scholten T. (2021) Improving the spatial prediction of soil salinity in arid regions using
550 wavelet transformation and support vector regression models. *Geoderma* 383:21. DOI:
551 10.1016/j.geoderma.2020.114793.
- 552 van der Kaars S., Tapper N., Cook E.J. (2010) Observed relationships between El Nino-Southern Oscillation, rainfall
553 variability and vegetation and fire history on Halmahera, Maluku, Indonesia. *Global Change Biology*
554 16:1705-1714. DOI: 10.1111/j.1365-2486.2009.02025.x.
- 555 Wei X.T., Huang S.Z., Huang Q., Leng G.Y., Wang H., He L., Zhao J., Liu D. (2021) Identification of the interactions
556 and feedbacks among watershed water-energy balance dynamics, hydro-meteorological factors, and
557 underlying surface characteristics. *Stochastic Environmental Research and Risk Assessment* 35:69-81. DOI:
558 10.1007/s00477-020-01896-9.
- 559 Wilcox J.M. (1976) Solar structure and terrestrial weather. *Science* (New York, N.Y.) 192:745-8. DOI:
560 10.1126/science.192.4241.745.
- 561 Willmott C.J., Matsuura K. (2001) Terrestrial Air Temperature and Precipitation: Monthly and Annual Time Series
562 (1950 - 1999). http://climate.geog.udel.edu/~climate/html_pages/README.ghec_ts2.html.
- 563 Wood T., Maycock A.C., Forster P.M., Richardson T.B., Andrews T., Boucher O., Myhre G., Samset B.H., Kirkevag
564 A., Lamarque J.F., Muelmenstaedt J., Olivi D., Takemura T., Watson-Parris D. (2020) The Southern
565 Hemisphere Midlatitude Circulation Response to Rapid Adjustments and Sea Surface Temperature Driven
566 Feedbacks. *Journal of Climate* 33:9673-9690. DOI: 10.1175/jcli-d-19-1015.1.
- 567 Xu T., Zhu L., Ma Q., Wang J., Lu X., Tang L. (2021) Moisture and vegetation variations in the extremely cold-dry
568 area of the Tibetan Plateau during the past 5000 years. *Catena* 204. DOI: 10.1016/j.catena.2021.105381.
- 569 Yetemen O., Saco P.M., Istanbuluoglu E. (2019) Ecohydrology Controls the Geomorphic Response to Climate
570 Change. *Geophysical Research Letters* 46:8852-8861. DOI: 10.1029/2019gl083874.

- 571 Zhang J.Z. (2021) Global patterns of phosphorus transformation in relation to latitude, temperature and precipitation.
572 *Pedosphere* 31:214-220. DOI: 10.1016/s1002-0160(20)60063-7.
- 573 Zhang X.Z., Chen J.Z., Song S.F. (2021) Divergent impacts of land use/cover change on summer precipitation in
574 eastern China from 1980 to 2000. *International Journal of Climatology* 41:2360-2374. DOI:
575 10.1002/joc.6963.
- 576 Zheng Y.H., Ganushkina N.Y., Jiggins P., Jun I., Meier M., Minow J.I., O'Brien T.P., Pitchford D., Shprits Y., Tobiska
577 W.K., Xapsos M.A., Guild T.B., Mazur J.E., Kuznetsova M.M. (2019) Space Radiation and Plasma Effects
578 on Satellites and Aviation: Quantities and Metrics for Tracking Performance of Space Weather Environment
579 Models. *Space Weather-the International Journal of Research and Applications* 17:1384-1403. DOI:
580 10.1029/2018sw002042.
- 581 [Data] Bureau of Meteorology. Southern Oscillation Index (SOI) data;
582 <http://www.bom.gov.au/climate/current/soi2.shtml>.
- 583 [Data] Royal Observatory of Belgium. Sunspot Index and Long-term Solar Observations data;
584 <http://sidc.oma.be/silso/monthlyssnplot>.
- 585 [Data] Willmott C J and Matsuura K. Terrestrial Air Temperature and Precipitation: Monthly and Annual Time Series
586 (1950 - 1999). 2001; http://climate.geog.udel.edu/~climate/html_pages/README.ghcns2.html.
- 587 [Data] University of Delaware Air Temperature & Precipitation.
588 https://www.psl.noaa.gov/data/gridded/data.UDel_AirT_Precip.html
589



590

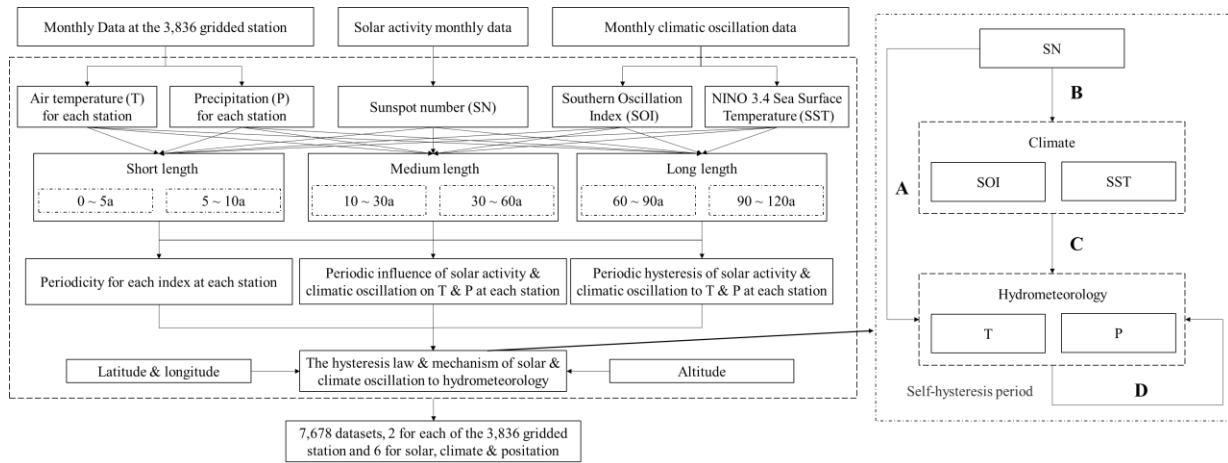
591 **Figure 1.** Schematic diagram of regional temperature and precipitation under the combined
592 influence of solar activity and climatic oscillation.



593

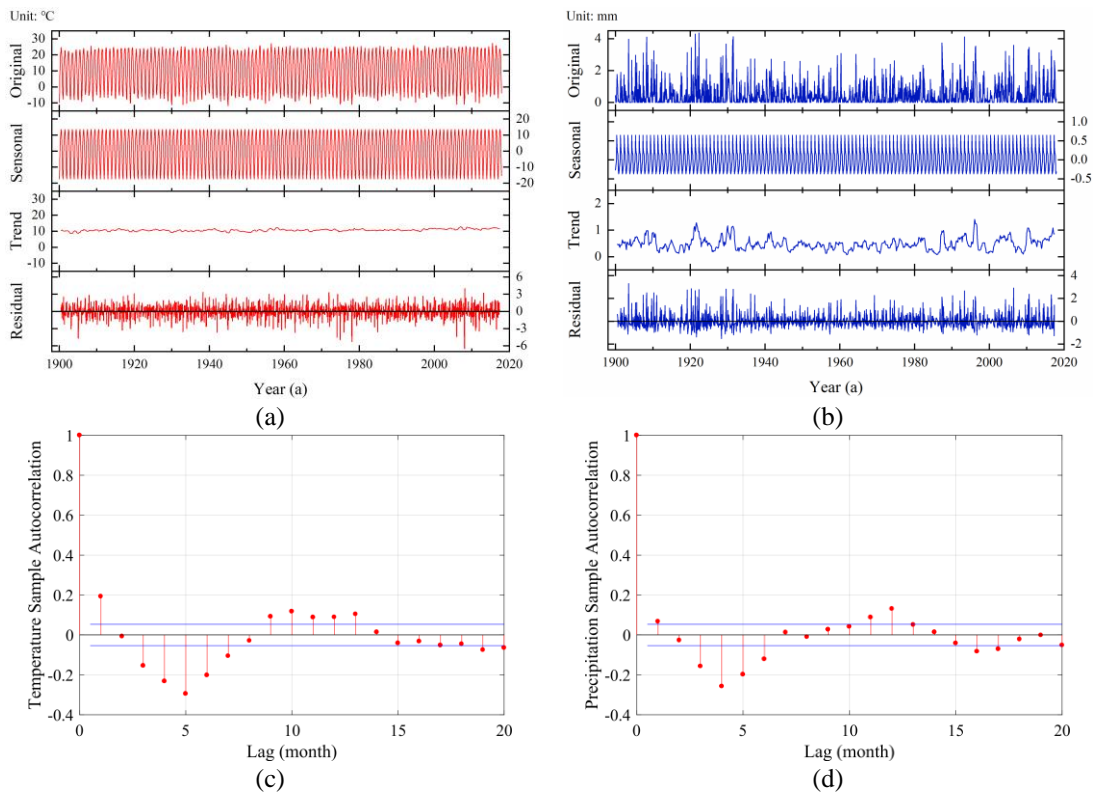
594 **Figure 2.** Map of the study region indicating the locations of the 3836 monthly global grid high-
595 resolution stations.

596

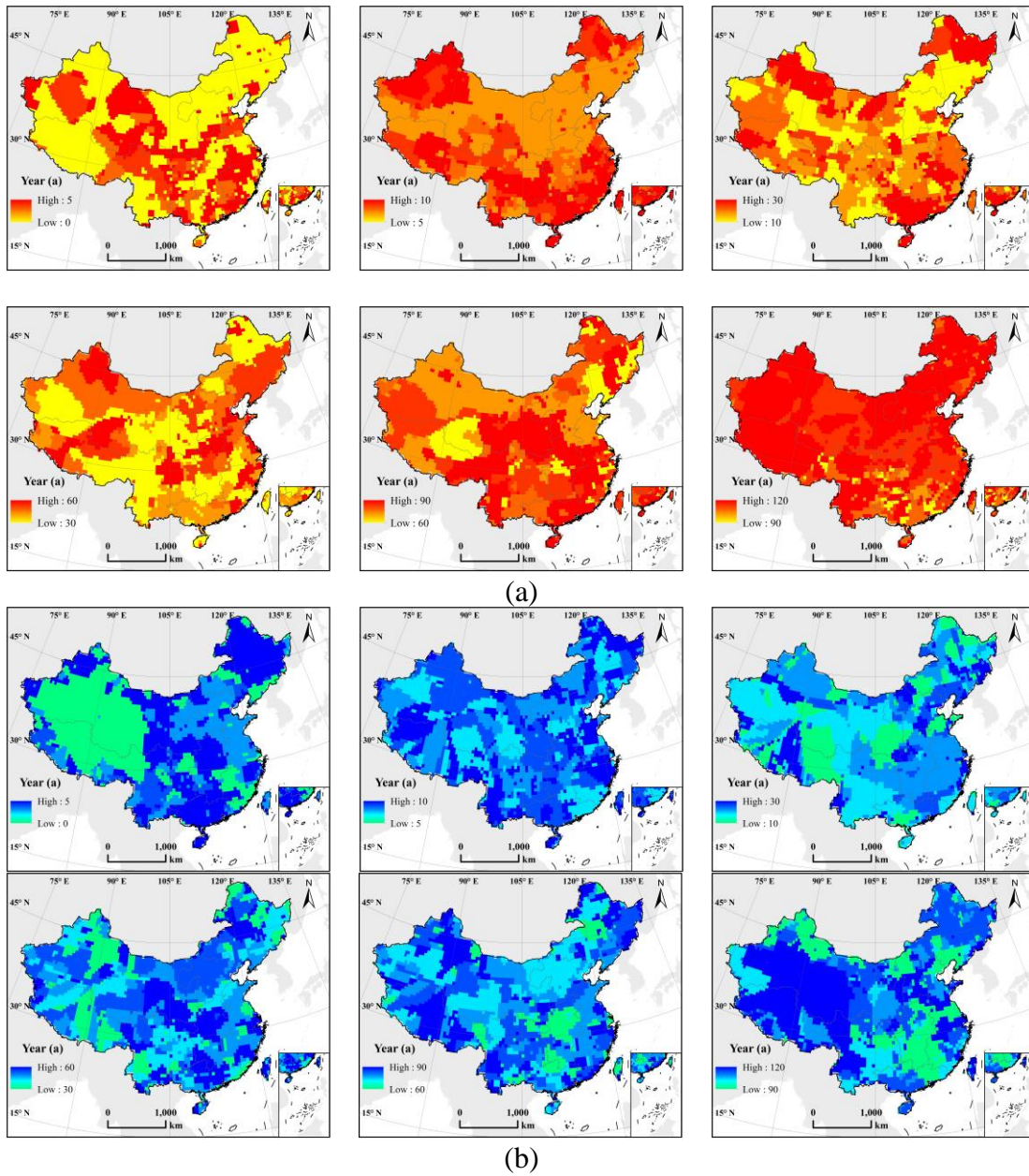


597

598 **Figure 3.** Flowchart showing the derivation of datasets from the data on daily T, P, SN, SOI, and
 599 SST, and their interaction mechanism. SN: sunspot number; SOI: southern oscillation index; SST:
 600 NINO 3.4 sea surface temperature.
 601

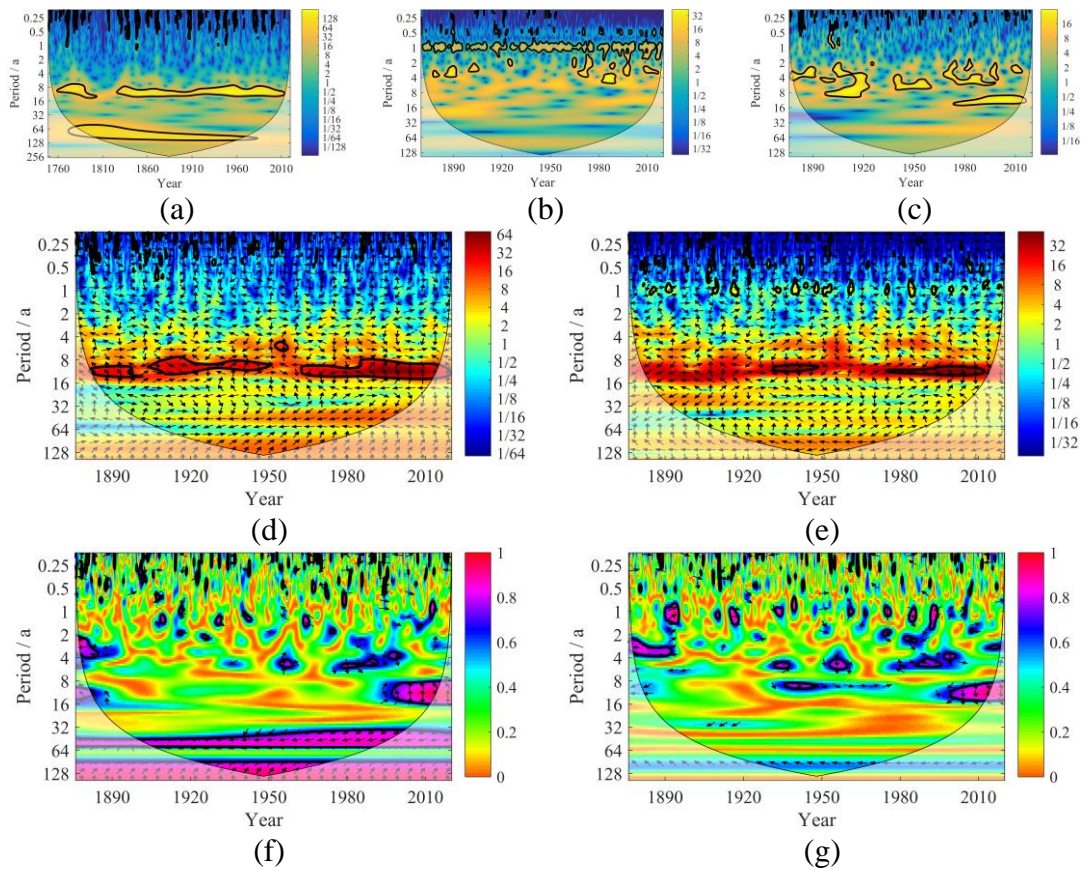


603 **Figure 4.** The original, seasonal, trend and residual terms of T (a) and P (b) by seasonal and trend
 604 decomposition using loess method (STL) and the autocorrelation using the residual terms of T (c)
 605 and P (d) by STL. Graph shows the data preprocessing of the sample grid station of China, and
 606 this method is applied to all station data used in the study.
 607

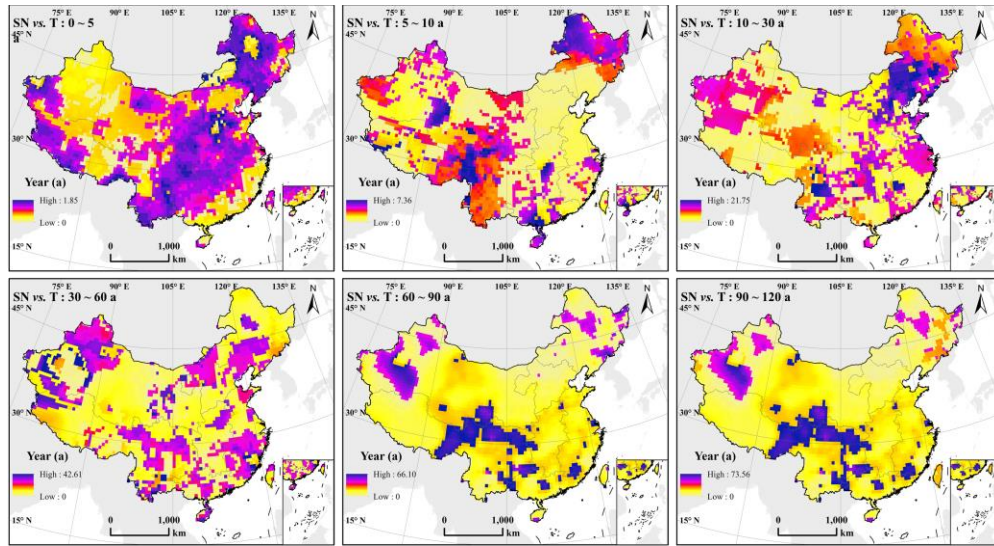


608 **Figure 5.** Gridded, latitude and longitude scale distribution of (a) T and (b) P periodicity of China
 609 under six periodic scales (1900–2020).
 610

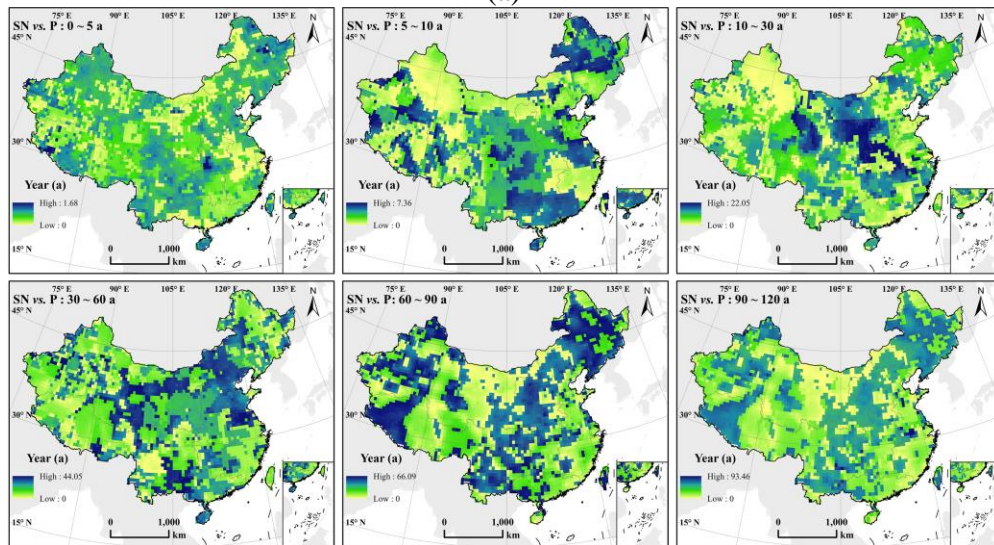
611



612 **Figure 6.** Continuous wavelet spectra of SN, SOI and SST (a-c). Cross wavelet transforms and
 613 wavelet coherences between SN and SOI (d, f), SST (e, g). (The thin solid line represents the
 614 wavelet influence cone, the thick solid line represents the horizontal interval of 5 % significance,
 615 the right arrow represents the concentric phase relationship, and the left arrow represents the
 616 inverse phase relationship.)
 617



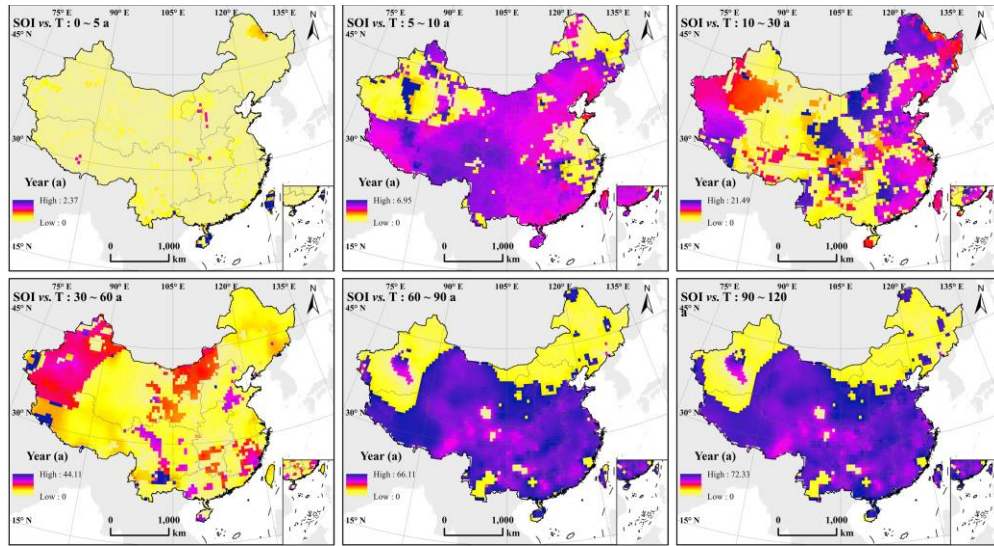
(a)



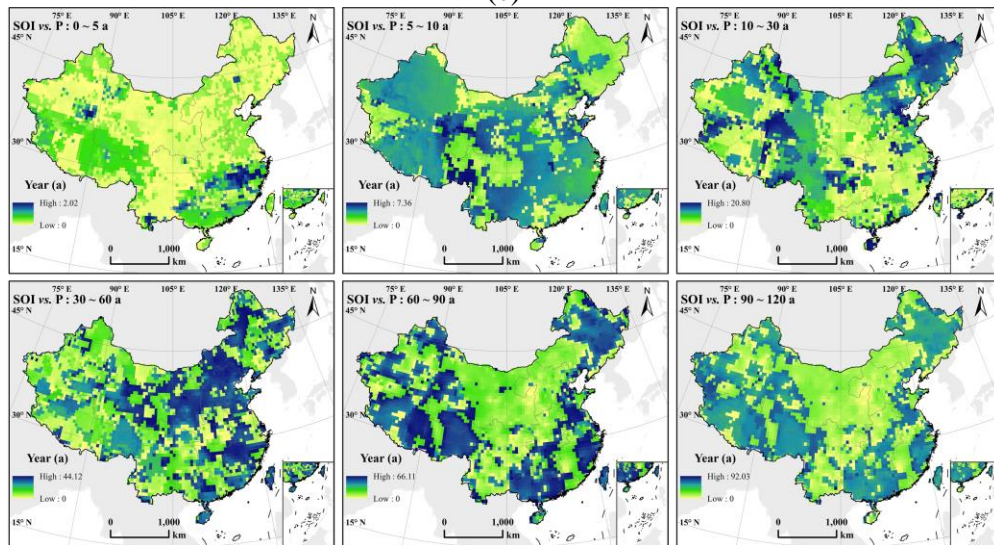
(b)

618
619

620
621



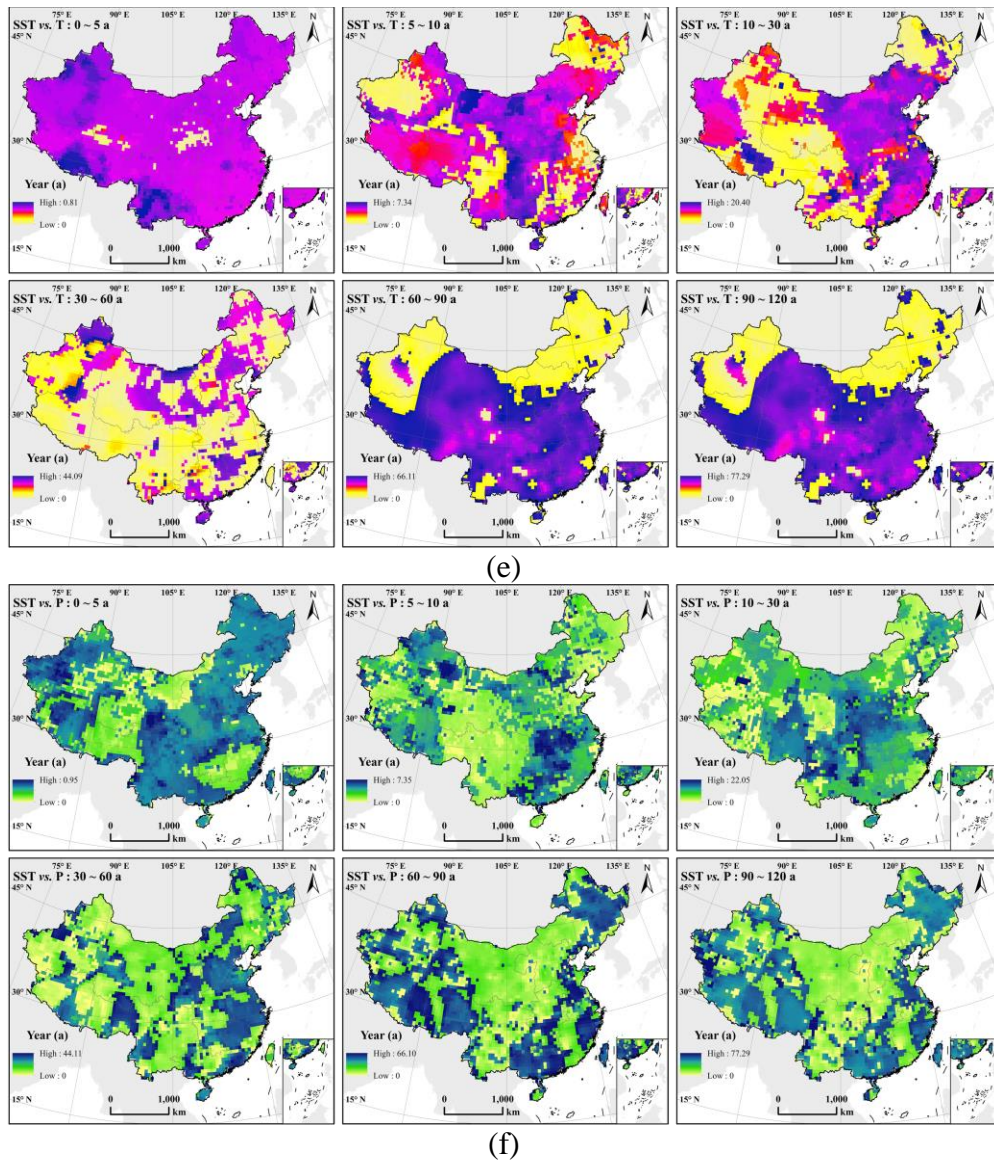
(c)



(d)

622
623

624
625

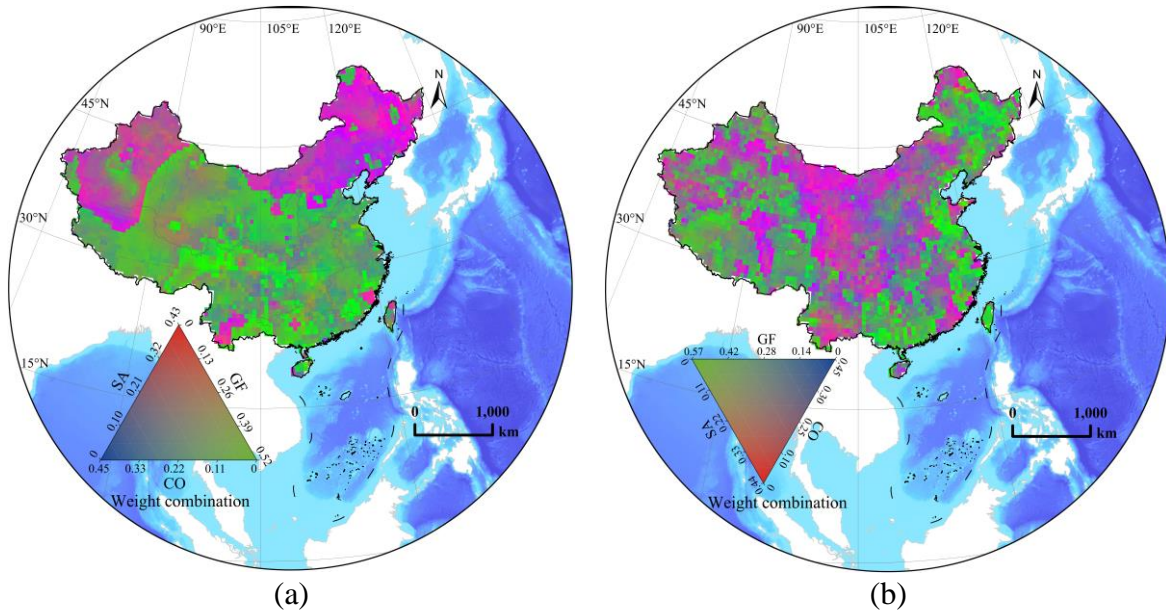


626
627

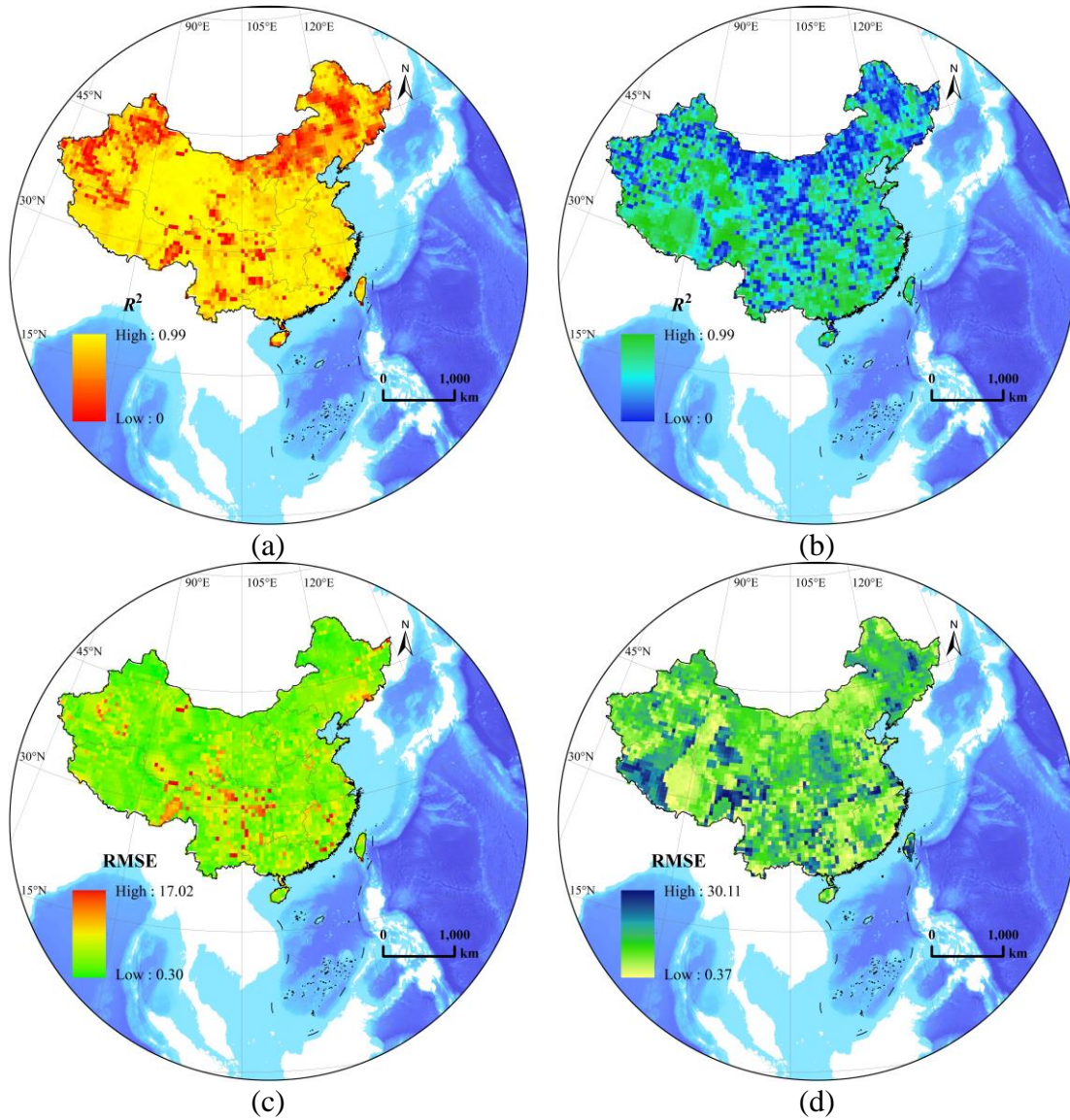
628
629

630 **Figure 7.** The significant lag period distributions of SN (a, b), SOI (c, d) and SST (e, f) to T and
631 P of China under six periodic scales (The significance level = 0.95).
632

633

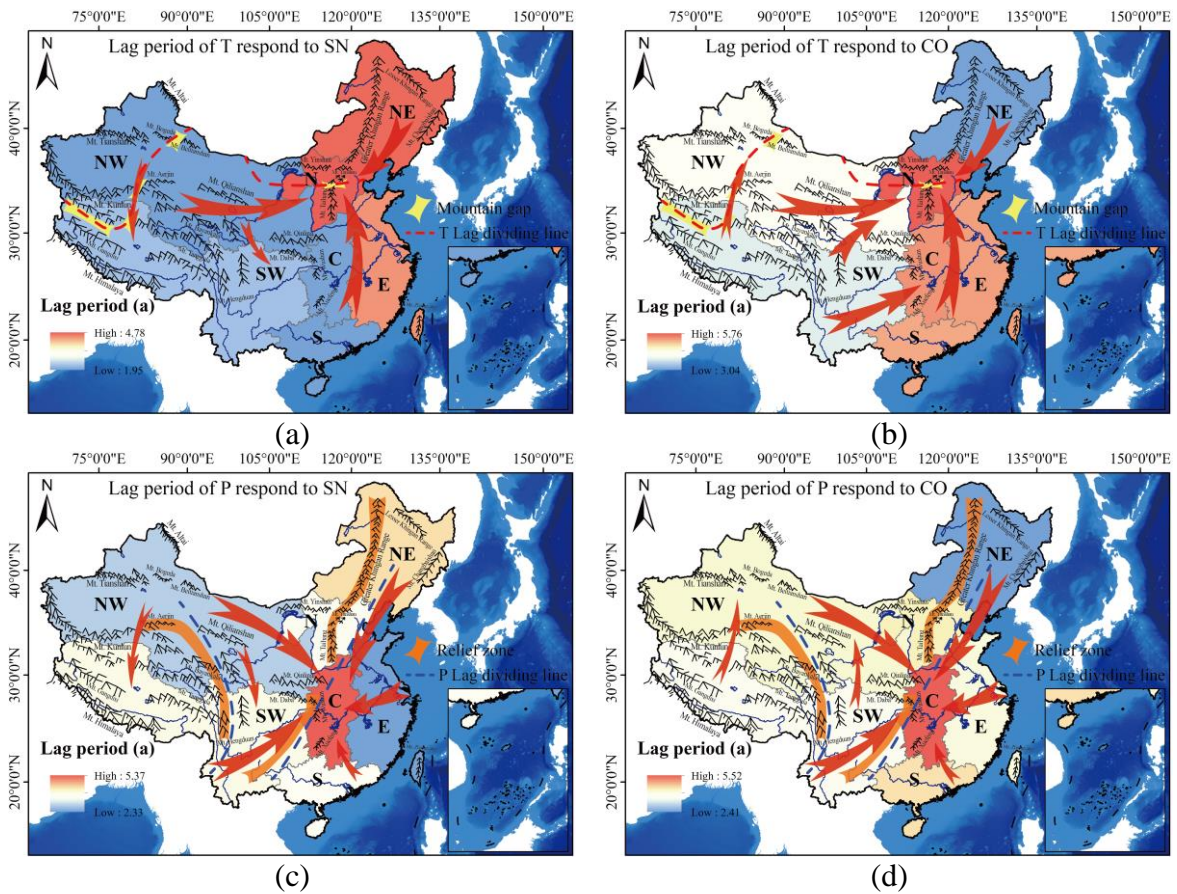


634 **Figure 8.** Entropy weight of SA, CO, and regional GF to the periodic hysteresis of T (a) and P (b)
 635 under six periodic scales in China. Red, blue, and green represent SA, CO, and GF, respectively
 636 (significance level = 0.95).
 637



639 **Figure 9.** Accuracy (a, b) and error (c, d) analysis of simulated T (a, c) and P (b, d) hysteresis
 640 period distribution using multivariate hysteretic decomposition model (MHD model; Eq.1). RMSE:
 641 root mean squared error (The significance level = 0.95).
 642

643



644 **Figure 10.** Theoretical diagram of the variation of (a, b) T and (c, d) P on the hysteresis period
 645 distribution of (a, c) SN and (b, d) CO. NW: Northwest China; N: North China; SW: Southwest
 646 China; E: Eastern China; C: Central China; S: South China.
 647

648 **Table 1.** Utilized information and number of T, N, SN, SOI, SST, SEA and DEM data in the
 649 research. T: air temperature; P: precipitation; SN: sunspot number; SOI: southern oscillation
 650 index; SST: NINO 3.4 sea surface temperature; SEA: solar elevation angle; DEM: digital
 651 elevation model.

Observation Items	Longitude (°E)	Latitude (°N)	Observation Time	Number of Data
T	69.25-129.25	18.75-53.25	1900-01/2020-12	3836*1428
P	69.25-129.25	18.75-53.25	1900-01/2020-12	3836*1428
SN	-	-	1749-01/2020-12	3264
SOI	-	-	1876-01/2020-12	1740
SST	-	-	1870-01/2020-12	1812
SEA	69.25-129.25	18.75-53.25	1900-01/2020-12	3836*1428
DEM	69.25-129.25	18.75-53.25	-	3836

652
653

Supporting Information for

Spatiotemporal Hysteresis Distribution and Decomposition of Solar Activities and Climatic Oscillation during 1900–2020

Mingyang Li¹, Tingxi Liu^{1,*}, Long Ma^{1,*}, Limin Duan¹, Yixuan Wang¹, Guoqiang Wang²,
Huimin Lei³, Vijay Singh⁴

¹ Inner Mongolia Water Resource Protection and Utilization Key Laboratory; Water Conservancy and Civil Engineering College, Inner Mongolia Agricultural University, Hohhot 010018, China;

² College of Water Sciences, Beijing Normal University, Beijing 100875, China;

³ State Key Laboratory of Hydrosience and Engineering, Department of Hydraulic Engineering, Tsinghua University, Beijing 100084, China;

⁴ Department of Biological and Agricultural Engineering & Zachry Department of Civil Engineering, Texas A&M University, College Station, TX 77843, USA).

Contents of this file

Figures S1 to S3

Tables S1 to S5

Introduction

In the "sun-climate-water resource" system, meteorological elements have different lag periods for influence factors such as solar activity (SA), climate oscillation (CO) and geographical factors (GF) at different spatiotemporal scales. However, this phenomenon has been insufficiently investigated. It is unclear whether the strong interaction/lag behaviours of meteorological elements responses to SA/CO that were calculated, statistically true and realistically possible. There is also insufficient information regarding the reasons and their weights for lag variation in different regions. Moreover, the transmission mechanism of the lag is also unclear. To overcome this knowledge gap, we studied temperature (T) and precipitation (P) data collected over 121 years from 3,836 grid stations across China. The spatial distribution of T and P, strong interaction periodic distribution responses to SA and CO, and hysteresis distribution were studied under six periodic scales (0–5, 5–10, 10–30, 30–60, 60–90, and 90–120 a), the. The weight distribution of lag influencing factors was plotted using false colour RGB to represent SA, GF, and CO; a multivariate hysteresis decomposition model was proposed to simulate and quantitatively decompose the periodic lag considering the factors of the earth's revolution.

We found that the strong interaction/lag period obtained on a long-time scale can be decomposed into several short, strong interaction/lag periods which are shorter than the SA period (11.2 a). The distribution of strong interaction and lag period is nested with the terrain and varies with the city. Additionally, regional underlying surface conditions and urbanisation significantly affect the lag periods of T and P.

There are two distinct dividing lines for the lag periods of T and P and patterns of influencing factors. The dividing lines for T run through valleys where water veins or mountains meet and gaps facilitate the cross-regional flow of monsoons. The two dividing lines are the Central Gobi–Ordos Plateau–Hengshan–Yanshan and the southern foot of the northern Tibetan Plateau–Cherchen River–Turpan Basin. The dividing line for P runs through the region where terrain changes drastically. Tall mountains of the Greater Hinggan–Taihang–Wushan–Xuefeng Mountains and Qilian–Bayankela–Hengduan Mountains block water vapour transportation. Regarding T lag trends, the northern region of China displays the longest lag period; the lag period of surrounding regions tends to converge toward the northern region. The lag period caused by sunspot numbers (SN) in Southwest China is larger than that in Northwest China, while the hysteresis effect of CO is opposite in the two regions. The hysteresis trend of P also has similar characteristics; the difference is that central China has the longest lag period.

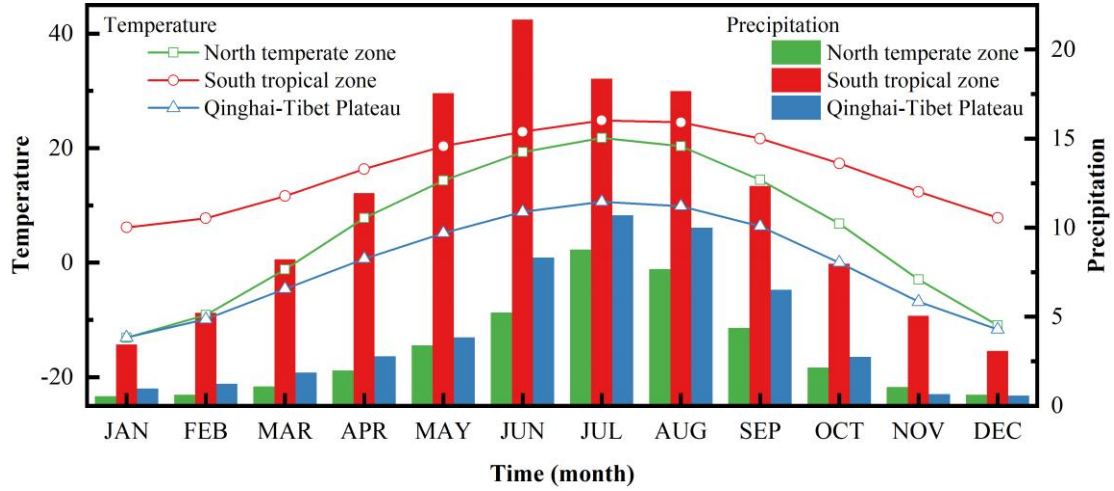
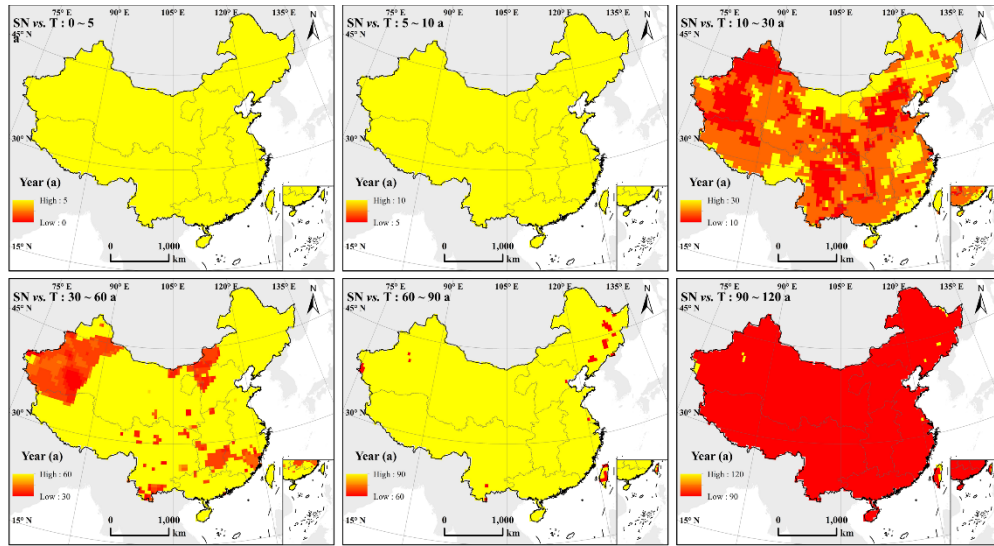
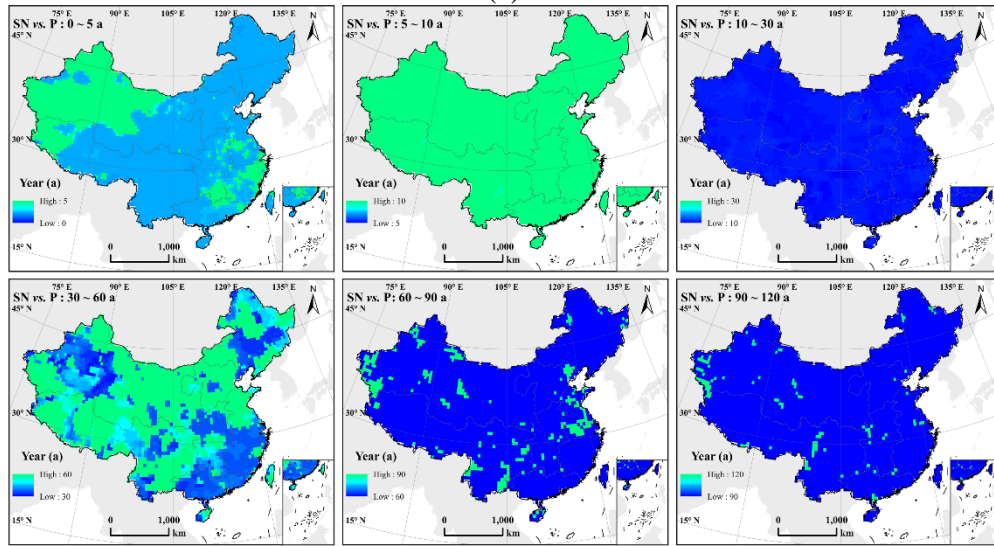


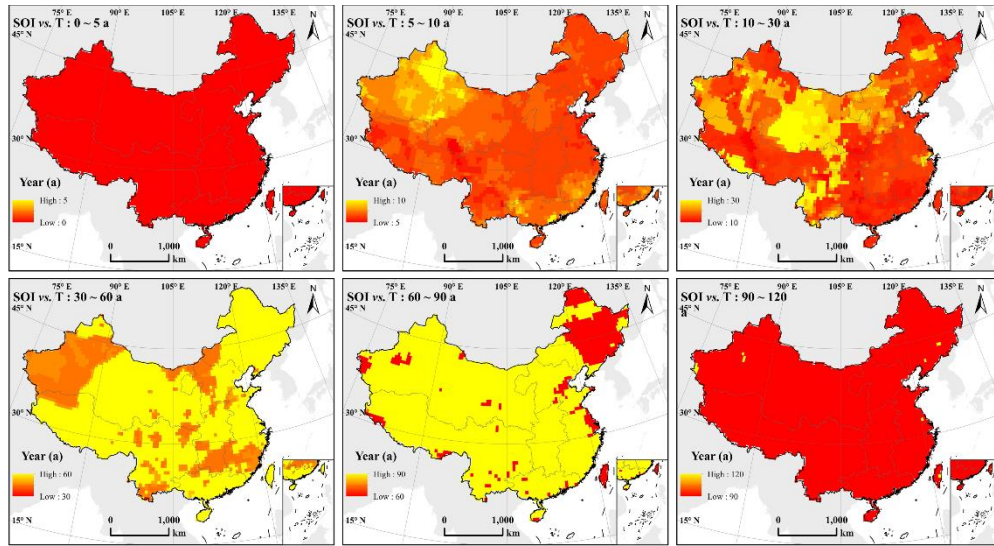
Figure S1. Plot showing T and P in north temperate zone, south tropical zone and Qinghai-Tibet plateau of China for the period 1900 to 2020.



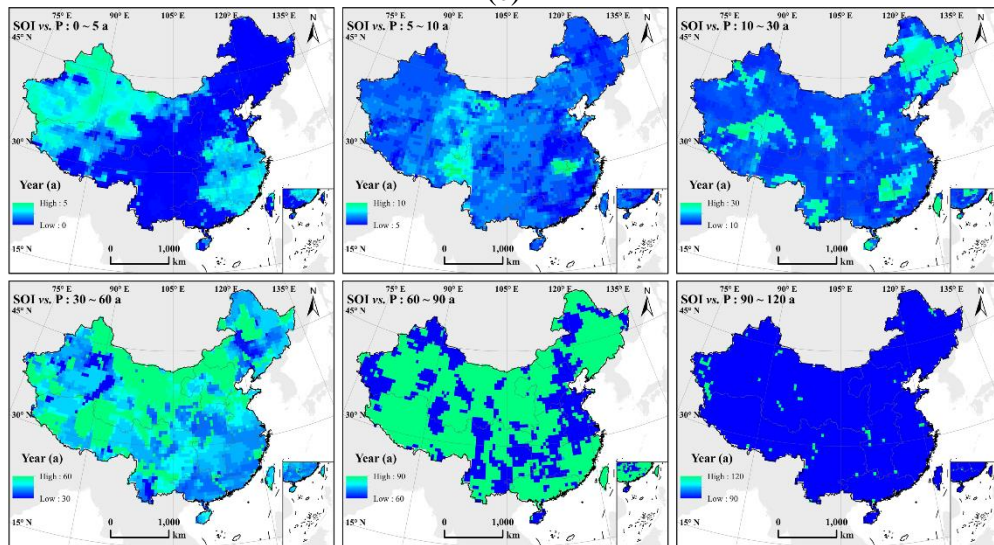
(a)



(b)



(c)



(d)

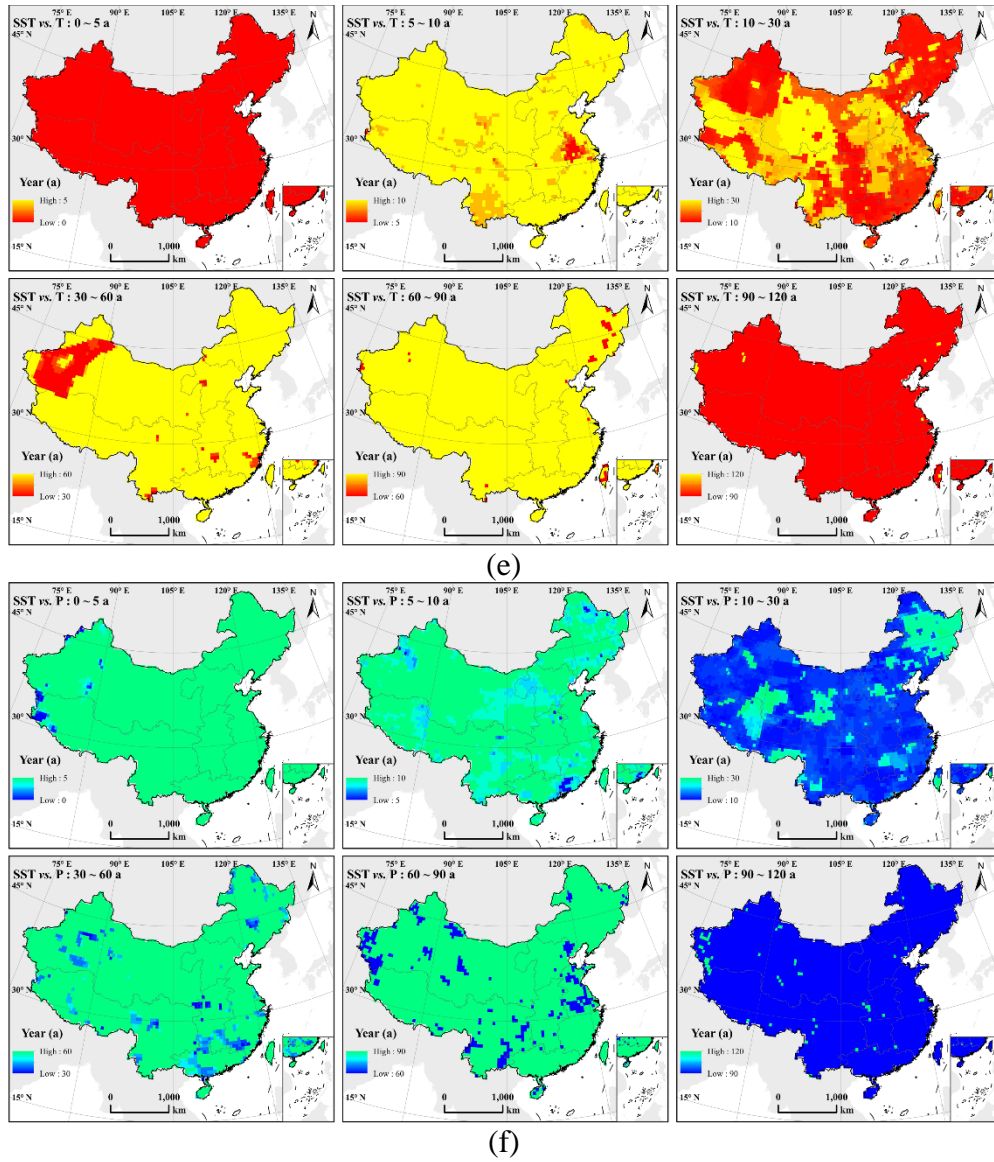


Figure S2. The significant periodic distributions of SN, SOI and SST to T (a, c, e) and P (b, d, f) of China under six periodic scales (The significance level = 0.95).

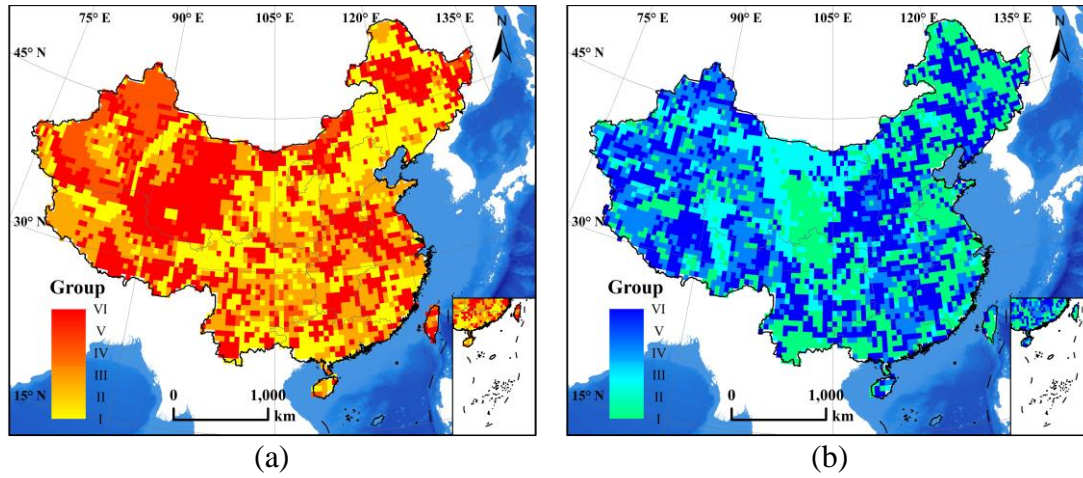


Figure S3. The hysteresis grouping distribution of T (a) and P (b) related to SA, CO, and GF of China using entropy weight under six periodic scales.

Supporting Information for

Spatiotemporal Hysteresis Distribution and Decomposition of Solar Activities and Climatic Oscillation during 1900–2020

Mingyang Li¹, Tingxi Liu^{1,*}, Long Ma^{1,*}, Limin Duan¹, Yixuan Wang¹, Guoqiang Wang²,
Huimin Lei³, Vijay Singh⁴

¹ Inner Mongolia Water Resource Protection and Utilization Key Laboratory; Water Conservancy and Civil Engineering College, Inner Mongolia Agricultural University, Hohhot 010018, China;

² College of Water Sciences, Beijing Normal University, Beijing 100875, China;

³ State Key Laboratory of Hydrosience and Engineering, Department of Hydraulic Engineering, Tsinghua University, Beijing 100084, China;

⁴ Department of Biological and Agricultural Engineering & Zachry Department of Civil Engineering, Texas A&M University, College Station, TX 77843, USA).

Contents of this file

Figures S1 to S3

Tables S1 to S5

Table S1. Median strong interaction periods between SN and T and P in seven regions of China (The significance level = 0.95).

Element Period (a)	T						Element Period (a)	P					
	0 ~ 5	5 ~ 10	10 ~ 30	30 ~ 60	60 ~ 90	90 ~ 120		0 ~ 5	5 ~ 10	10 ~ 30	30 ~ 60	60 ~ 90	90 ~ 120
NE	0.97	9.82	11.02	55.53	83.21	88.15	NE	1.03	9.82	11.02	55.53	83.21	88.15
NW	0.97	9.82	11.02	55.53	83.21	88.15	NW	1.03	9.82	11.02	55.53	83.21	88.15
N	0.97	9.82	9.82	55.53	83.21	88.15	N	1.03	9.82	11.02	55.53	83.21	88.15
SW	0.97	9.82	11.02	55.53	83.21	88.15	SW	1.03	9.82	11.02	55.53	83.21	88.15
E	0.97	9.82	11.02	55.53	83.21	88.15	E	1.03	9.82	11.02	55.53	83.21	88.15
C	0.97	9.82	11.02	55.53	83.21	88.15	C	1.03	9.82	11.02	34.98	83.21	88.15
S	0.97	9.82	11.02	55.53	83.21	88.15	S	1.03	9.82	11.02	55.53	83.21	88.15

Note: NE: Northeast China; NW: Northwest China; N: North China; SW: Southwest China; E: Eastern China; C: Central China; S: South China.

Table S2. Median strong interaction periods between CO and T and P in seven regions of China (The significance level = 0.95).

Element Period (a)	T						Element Period (a)	P					
	0 ~ 5	5 ~ 10	10 ~ 30	30 ~ 60	60 ~ 90	90 ~ 120		0 ~ 5	5 ~ 10	10 ~ 30	30 ~ 60	60 ~ 90	90 ~ 120
NE	1.03	9.82	11.02	58.84	83.21	88.15	NE	1.03	9.82	20.80	58.84	83.21	88.15
NW	1.03	9.82	20.80	58.84	83.21	88.15	NW	1.03	9.82	11.02	58.84	83.21	88.15
N	1.03	9.82	19.63	58.84	83.21	88.15	N	1.03	9.82	11.02	58.84	83.21	88.15
SW	1.03	9.82	19.63	58.84	83.21	88.15	SW	1.03	9.82	11.02	58.84	83.21	88.15
E	1.03	9.82	11.02	58.84	83.21	88.15	E	1.03	9.82	11.02	58.84	83.21	88.15
C	1.03	9.27	18.53	58.84	83.21	88.15	C	1.03	9.82	11.02	58.84	83.21	88.15
S	1.03	9.82	11.02	58.84	83.21	88.15	S	1.03	9.82	10.40	58.84	83.21	88.15

Table S3. Median hysteresis periods between SN and T and P in seven regions of China (The significance level = 0.95).

Element Period (a)	T						Element Period (a)	P					
	0 ~ 5	5 ~ 10	10 ~ 30	30 ~ 60	60 ~ 90	90 ~ 120		0 ~ 5	5 ~ 10	10 ~ 30	30 ~ 60	60 ~ 90	90 ~ 120
NE	0.64	3.58	8.91	7.97	5.71	6.66	NE	0.54	4.08	6.67	20.18	50.79	53.66
NW	0.25	1.66	4.02	7.30	16.35	17.62	NW	0.45	1.39	6.25	19.80	19.97	22.25
N	0.51	0.50	13.32	9.42	8.95	9.89	N	0.45	1.96	7.25	31.92	45.25	47.31
SW	0.56	2.61	3.58	8.60	16.71	18.05	SW	0.40	3.51	6.38	10.43	21.43	22.18
E	0.49	1.03	10.78	11.15	17.72	19.17	E	0.25	1.95	4.82	21.49	14.20	15.80
C	0.62	0.77	4.55	6.32	18.08	19.31	C	0.38	3.18	12.54	21.43	17.52	20.37
S	0.24	1.88	3.79	8.37	18.67	20.21	S	0.22	5.48	4.12	25.14	18.92	19.57

Table S4. Median hysteresis periods between CO and T and P in seven regions of China (The significance level = 0.95).

Element Period (a)	T						Element Period (a)	P					
	0 ~ 5	5 ~ 10	10 ~ 30	30 ~ 60	60 ~ 90	90 ~ 120		0 ~ 5	5 ~ 10	10 ~ 30	30 ~ 60	60 ~ 90	90 ~ 120
NE	0.54	4.08	6.67	20.18	50.79	53.66	NE	0.55	1.58	5.13	13.03	46.40	47.44
NW	0.45	1.39	6.25	19.80	19.97	22.25	NW	0.47	3.46	8.31	11.31	17.86	18.79
N	0.45	1.96	7.25	31.92	45.25	47.31	N	0.54	3.73	8.53	33.00	14.54	15.10
SW	0.40	3.51	6.38	10.43	21.43	22.18	SW	0.55	1.53	8.90	9.56	44.97	50.36
E	0.25	1.95	4.82	21.49	14.20	15.80	E	0.55	3.66	7.78	34.80	52.11	59.47
C	0.38	3.18	12.54	21.43	17.52	20.37	C	0.55	5.80	10.21	26.95	18.45	21.34
S	0.54	4.08	6.67	20.18	50.79	53.66	S	0.58	4.17	8.34	28.82	54.77	56.86

Table S5. Multivariate hysteretic decomposition (MHD) model parameters under six periodic scales (The significance level = 0.95).

Period	Group	α_1	α_2	τ_1	τ_2	τ_3	ρ_1	ρ_2	ρ_3	δ
0 to 5 a	I	-0.5165	0.0672	-0.0003	0.0037	0.1664	0.0015	-0.0004	0.0151	0.1922
	II	-0.8189	0.1571	0.0035	-0.077	0.2691	-0.0021	0.0017	-0.0083	0.2917
	III	-1.5205	0.1857	-0.0031	-0.0986	0.6459	-0.0026	0.0009	0.0104	0.6569
	IV	-1.4135	-0.1058	-0.0131	-0.1811	0.5978	-0.0005	0.0013	0.0057	0.6103
	V	-1.2227	-0.0835	-0.0044	0.0188	0.4902	0.0021	0.0007	0.0004	0.506
	VI	-0.5373	0.0269	-0.0005	-0.0392	0.1085	0.0021	0.001	0.0033	0.136
5 to 10 a	I	0.8059	-0.0472	-0.0001	-0.2463	-0.1471	0.0131	-0.0077	0.0004	-6.0461
	II	-0.189	-1.8573	0.0004	0.1298	-0.464	0.0016	0.0231	-0.1027	4.3298
	III	-0.6629	1.1034	0.0002	0.0077	0.2756	0.031	0.0066	-0.2605	2.5912
	IV	-0.58	-4.5186	0.0007	-0.2701	-0.2432	-0.0264	0.0134	-0.1786	9.2226
	V	-0.1348	-3.5601	-0.002	-0.1631	0.1565	-0.0306	0.001	0.1656	2.2969
	VI	-1.2865	-1.086	-0.0027	0.28	0.0329	-0.0311	0.0069	-0.0339	13.4102
10 to 30 a	I	0.2315	-1.2554	0.0021	-0.4587	-0.105	-0.0581	0.0668	-0.1314	-2.8077
	II	0.2352	2.6913	0.0048	-0.6032	-0.1971	-0.0335	0.0736	0.1925	-9.0533
	III	0.4548	2.7071	0.0028	-0.3443	-0.0733	-0.0049	-0.0072	0.0409	-2.1104
	IV	1.4141	17.7787	-0.0006	-0.0886	-0.1039	-0.0177	0.046	0.3451	-26.8089
	V	0.194	-0.2865	-0.0038	-0.5235	-0.0385	-0.0171	0.0045	-0.1391	-0.5154
	VI	0.4721	5.3347	-0.0014	-0.08	-0.106	0.033	0.0195	0.1975	-9.4731
30 to 60 a	I	0.0233	2.433	-0.0008	0.1103	-0.0919	0.1342	-0.0044	0.8493	0.6378
	II	-0.1686	2.8135	-0.0014	-0.0978	0.2431	0.2215	-0.0254	0.7189	-8.9337
	III	-0.1376	0.8498	-0.0009	0.1751	0.2351	0.2181	-0.0351	0.2493	-10.0245
	IV	-0.0661	30.8438	0.0014	0.186	-0.1769	0.077	-0.1889	1.9328	15.2735
	V	0.1444	21.1293	0.0004	-0.2047	-0.1737	0.0302	-0.0852	-0.277	1.4021
	VI	0.1229	-1.2327	0.0012	0.3299	0.0999	0.0225	-0.0849	0.9941	-2.7241
60 to 90 a	I	-0.5816	8.7484	-0.0015	-0.9798	0.4221	0.3244	-0.2857	0.3081	29.5432
	II	0.1414	14.1589	0.0003	-1.2022	0.0045	-0.2668	-0.1357	-0.0936	-1.6696
	III	-0.4225	6.0583	0.0013	-2.3243	0.2678	-0.0184	-0.0948	-0.7904	-11.8956

	IV	-0.0763	1.6957	0.0001	1.3275	0.001	0.0077	0.0099	-0.0699	-14.8342
	V	-0.4238	-1.8188	-0.0006	1.107	0.0158	-0.0235	0.0001	0.0118	19.7606
	VI	-0.0528	2.9651	-0.0026	-0.8805	0.1928	0.1194	-0.068	-0.0392	-3.088
90 to 120 a	I	0.2785	10.4859	-0.0012	-1.1341	0.3032	0.2434	-0.2986	0.3848	-34.3641
	II	-20.8869	18.8804	0.0004	-1.4547	21.5393	-0.2606	-0.1365	-0.3835	-52.9784
	III	-0.2027	8.8825	0.001	-2.3945	-0.2035	0.0498	-0.0543	-0.8099	0.9864
	IV	1.9471	9.0987	0.0013	-0.1843	-1.5884	-0.2994	-0.0849	-0.0563	-3.878
	V	0.6615	-9.3078	0.0003	0.162	-0.0259	-0.1945	-0.0454	0.2027	-39.8326
	VI	0.2029	-5.9463	-0.0021	-0.8335	-0.0458	0.055	-0.0864	-0.0702	2.6432

Note: I to VI are the groups in Supplementary Figure S3.